

Turbulent density and pressure fluctuations in the stratified intracluster medium

Rajsekhar Mohapatra¹★, Christoph Federrath^{1,2}† and Prateek Sharma³‡

¹Research School of Astronomy and Astrophysics, Australian National University, Canberra, ACT 2611, Australia

²Australian Research Council Centre of Excellence in All Sky Astrophysics (ASTRO3D), Canberra, ACT 2611, Australia

³Department of Physics, Indian Institute of Science, Bangalore, KA 560012, India

Accepted XXX. Received YYY; in original form ZZZ

ABSTRACT

Turbulent gas motions are observed in the intracluster medium (ICM). The ICM is density-stratified, with the gas density being highest at the centre of the cluster and decreasing radially outwards. As a result of this, Kolmogorov (homogeneous, isotropic) turbulence theory does not apply to the ICM. The gas motions are instead explained by anisotropic stratified turbulence, with the stratification quantified by the perpendicular Froude number (Fr_{\perp}). These turbulent motions are associated with density and pressure fluctuations, which manifest as perturbations in X-ray surface brightness maps of the ICM and as thermal Sunyaev-Zeldovich effect (SZ) fluctuations, respectively. In order to advance our understanding of the relations between these fluctuations and the turbulent gas velocities, we have conducted 100 high-resolution hydrodynamic simulations of stratified turbulence ($256^2 \times 384$ – $1024^2 \times 1536$ resolution elements), in which we scan the parameter space of subsonic rms Mach number (\mathcal{M}), Fr_{\perp} , and the ratio of entropy and pressure scale heights ($R_{PS} = H_P/H_S$), relevant to the ICM. We develop a new scaling relation between the standard deviation of logarithmic density fluctuations (σ_s , where $s = \ln(\rho/\langle\rho\rangle)$), \mathcal{M} , and Fr_{\perp} , which covers both the strongly stratified ($Fr_{\perp} \ll 1$) and weakly stratified ($Fr_{\perp} \gg 1$) turbulence regimes: $\sigma_s^2 = \ln(1 + b^2\mathcal{M}^4 + 0.10/(Fr_{\perp} + 0.25/\sqrt{Fr_{\perp}})^2\mathcal{M}^2R_{PS})$, where $b \sim 1/3$ for solenoidal turbulence driving studied here. We further find that logarithmic pressure fluctuations $\sigma_{(\ln P/\langle P \rangle)}$ are independent of stratification and scale according to the relation $\sigma_{(\ln \bar{P})}^2 = \ln(1 + b^2\gamma^2\mathcal{M}^4)$, where $\bar{P} = P/\langle P \rangle$ and γ is the adiabatic index of the gas. We have tested these scaling relations to be valid over the parameter ranges $\mathcal{M} = 0.01$ – 0.40 , $Fr_{\perp} = 0.04$ – 10.0 , and $R_{PS} = 0.33$ – 2.33 .

Key words: methods: numerical – hydrodynamics – turbulence – stratification – ICM – CGM

1 INTRODUCTION

Turbulence and buoyancy are concurrent in several geophysical and astrophysical systems – the physics of stratified turbulence governs ocean currents and atmospheric turbulence on the earth and other planets, radiative and convective zones in the atmospheres of the sun and other stars, gas motions in hot gaseous haloes of galaxies (the circumgalactic medium or CGM), galaxy groups and clusters (intracluster medium or ICM) (Stein 1967; Goldreich & Keeley 1977; Loewenstein & Fabian 1990; Sarazin et al. 1992; Rudie et al. 2012; Parmentier et al. 2013; Skoutnev et al. 2020). Here we focus on stratified turbulence relevant to the ICM.

ICM refers to the gas that pervades the region between galaxies in a cluster. It is mostly composed of the hot X-ray emitting gas,

with temperatures ranging from 10^7 – 10^8 K, although a filamentary colder phase has also been detected in many clusters (Cowie et al. 1983; McDonald et al. 2010; Simionescu et al. 2018; Vantyghem et al. 2019; Olivares et al. 2019). It is moderately stratified (with Richardson number $Ri \lesssim 10$ or Froude number $Fr_{\perp} \gtrsim 0.1$, refer to figure 1 in Mohapatra et al. 2020) and the gas is in rough hydrostatic equilibrium with the gravitational profile set by the dark matter halo. Turbulence in the ICM plays an important role in the gas dynamics and evolution. Turbulent energy dissipation on viscous scales and subsequent heating of the ICM, turbulent mixing of hot and cold phases of gas (Kim & Narayan 2003; Banerjee & Sharma 2014; Hillel & Soker 2020) may also play a key role in the gas thermodynamics, by preventing the runaway cooling of the ICM core (Zhuravleva et al. 2014a). Anisotropy in turbulent eddies may be used to probe the orientation of ICM magnetic fields (Hu et al. 2020). In cluster outskirts, estimating the turbulent pressure support of the gas is important to get an unbiased estimate of the halo mass that is required for cosmology with clusters (Schuecker et al. 2004;

★ E-mail: rajsekhar.mohapatra@anu.edu.au (RM)

† E-mail: christoph.federrath@anu.edu.au (CF)

‡ E-mail: prateek@iisc.ac.in (PS)

George et al. 2009; Bautz et al. 2009; Cavaliere et al. 2011; Nelson et al. 2014; Biffi et al. 2016; Angelinelli et al. 2020).

However, direct measurements of the ICM turbulent gas velocities (Hitomi Collaboration 2016) are still a few years away (XRISM¹ and Athena²), after the early mission end of the Hitomi satellite. Recently, observers have relied on several indirect methods to estimate gas velocities in the hot phase, such as relating X-ray surface brightness fluctuations to turbulent velocity fluctuations (Zhuravleva et al. 2014a, 2015, 2019), relating Sunyaev-Zeldovich effect (SZ) observations to turbulent pressure fluctuations (Zeldovich & Sunyaev 1969; Khatri & Gaspari 2016; Mroczkowski et al. 2019), measuring cold-gas velocities (e.g., using the H α line) and relating this to the hot phase velocity (Li et al. 2020). Simionescu et al. (2019) provide a detailed review of all these different methods of measuring gas velocities in the ICM. It is important to develop accurate and robust scaling relations between the ICM hot-gas velocities and these observables.

Many recent theoretical studies have focused on the scaling of density fluctuations with the rms Mach number (\mathcal{M}) (Gaspari et al. 2014; Zhuravleva et al. 2014b; Nolan et al. 2015; Mohapatra & Sharma 2019; Shi & Zhang 2019; Grete et al. 2020; Mohapatra et al. 2020). Some of these studies have ignored the effect of gravitational stratification or lack a detailed parameter scan of the range of Fr_\perp and \mathcal{M} relevant for the ICM. The relation between density fluctuations and turbulent velocities is also seen to depend on the equation of state of the gas (Federrath & Banerjee 2015) and the adiabatic index (Nolan et al. 2015), and whether gas cooling is included (Mohapatra & Sharma 2019; Grete et al. 2020).

Several fluid mechanics studies (Bolgiano 1959, 1962; Carnevale et al. 2001; Lindborg 2006; Brethouwer & Lindborg 2008; Herring & Kimura 2013; Kumar et al. 2014; Rorai et al. 2014; Feraco et al. 2018; Alam et al. 2019) discuss the theory of stratified turbulence in the context of planetary atmospheres and oceans. In these studies, turbulence is driven perpendicular to the direction of gravity, whereas turbulence in the ICM is driven more isotropically by active galactic nuclei (AGN) jets and galaxy mergers (Churazov et al. 2002, 2003; Omma et al. 2004). They also mainly focus on the scaling of velocity and passive scalar spectra, intermittency and velocity anisotropy in the strong stratification limit.

In our previous study (Mohapatra et al. 2020) (hereafter referred to as MFS20), we performed stratified turbulence simulations with a fixed \mathcal{M} and scanned the parameter space of weakly and moderately stratified turbulence. We also proposed a scaling relation between density fluctuations, Richardson number (Ri) and \mathcal{M} for this regime. We found that density fluctuations also depended on a third parameter, namely the ratio between pressure and entropy scale heights ($R_{PS} = H_P/H_S$). We found that for $\text{Ri} \lesssim 10$ (only moderately stratified), these numbers are sensitive to the turbulent driving length scale L , as $\text{Ri} \propto L^2$. Here we scan the parameter space of these three parameters: \mathcal{M} , the transverse Froude number Fr_\perp ($\text{Fr}_\perp \approx 1/\sqrt{\text{Ri}}$ for $\text{Fr}_\perp \gtrsim 1$) and R_{PS} through 100 simulations, extending into the strongly stratified regime ($\text{Fr}_\perp \ll 1$).

The paper is organised as follows. In section 2 we briefly describe our setup and methods, present our results and their interpretations in section 3, compare our results with the literature and discuss the caveats of our work in section 4, and conclude in section 5.

2 METHODS

2.1 Model equations

We model the ICM as a fluid using compressible Euler equations and ideal gas equation of state. We implement gravity and turbulent forcing as additional source terms in the momentum and energy equations. We solve the following equations:

$$\frac{\partial \rho}{\partial t} + \nabla \cdot (\rho \mathbf{v}) = 0, \quad (1a)$$

$$\frac{\partial (\rho \mathbf{v})}{\partial t} + \nabla \cdot (\rho \mathbf{v} \otimes \mathbf{v}) + \nabla P = \rho \mathbf{F} + \rho \mathbf{g}, \quad (1b)$$

$$\frac{\partial E}{\partial t} + \nabla \cdot ((E + P)\mathbf{v}) = \rho \mathbf{F} \cdot \mathbf{v} + \rho (\mathbf{v} \cdot \nabla) \Phi, \quad (1c)$$

where ρ is the gas mass density, \mathbf{v} is the velocity, $P = \rho k_B T / (\mu m_p)$ is the pressure (we use the ideal gas equation of state), \mathbf{F} is the turbulent acceleration that we apply, Φ is the gravitational potential, $\mathbf{g} = -\nabla \Phi$ is the acceleration due to gravity, $E = \rho v^2/2 + P/(\gamma - 1)$ is the sum of kinetic and internal energy densities, μ is the mean particle weight, m_p is the proton mass, k_B is the Boltzmann constant, T is the temperature, and $\gamma = 5/3$ is the adiabatic index.

2.2 Setup

We choose $-\hat{\mathbf{z}}$ to be the direction of the gravitational field, and pressure and density to have scale heights H_P and H_ρ , respectively. Thus, the initial pressure and density profiles are given by

$$P(t=0) = P_0 \exp\left(-\frac{z}{H_P}\right) \text{ and} \quad (2a)$$

$$\rho(t=0) = \rho_0 \exp\left(-\frac{z}{H_\rho}\right), \text{ respectively.} \quad (2b)$$

We work with dimensionless units and choose $\rho_0 = 1$ and $P_0 = 0.6$, so that $c_{s,0} = \sqrt{\gamma P_0/\rho_0} = 1$. Since we start with the gas in hydrostatic equilibrium, the initial density, pressure, and g , are related by

$$\frac{dP}{dz} = -\rho g. \quad (3a)$$

Hence g is set as

$$g = \frac{P_0}{\rho_0 H_P} \exp\left(-z \left[\frac{1}{H_P} - \frac{1}{H_\rho} \right]\right). \quad (3b)$$

This equilibrium is convectively stable if $d \ln S/dz > 0$, where

$$S = \frac{P}{\rho^\gamma} \text{ is the pseudo-entropy.} \quad (4)$$

This gives us the condition for the entropy scale height H_S ($\equiv 1/[d \ln S/dz]$), given by

$$\frac{1}{H_S} = \frac{\gamma}{H_\rho} - \frac{1}{H_P} > 0. \quad (5)$$

This condition is satisfied for all our simulations, which locally mimic the stably stratified ICM.

2.3 Important stratified turbulence parameters

When a parcel of gas in a stably stratified medium is displaced from its original position, it oscillates with a frequency N defined as the Brunt-Väisälä (BV) frequency, given by

$$N^2 = \frac{g}{\gamma} \frac{d}{dz} \ln \left(\frac{P}{\rho^\gamma} \right). \quad (6a)$$

¹ <https://global.jaxa.jp/projects/sas/xrism/>

² <https://www.the-athena-x-ray-observatory.eu/>

We define the turbulent time scale as ℓ_{\perp}/v_{\perp} , where ℓ_{\perp} is the integral scale, defined as

$$\ell_{\perp} = 2\pi \frac{\int k_{\perp}^{-1} E_{k_{\perp}} dk_{\perp}}{\int E_{k_{\perp}} dk_{\perp}}, \quad (6b)$$

$$v_{\perp} = \left\langle \frac{1}{2} \mathbf{v}_{\perp}^2 \right\rangle^{1/2}. \quad (6c)$$

Here $E_{k_{\perp}}$ is the velocity power spectrum perpendicular to the direction of \mathbf{g} . Here $\mathbf{v}_{\perp} = (v_x, v_y, 0)$ denotes the components of the velocity field perpendicular to the direction of gravity. The perpendicular Froude number Fr_{\perp} is the ratio of these two time scales (see e.g., chapter 14 in [Davidson 2013](#)), given as

$$\text{Fr}_{\perp} = \frac{v_{\perp}}{N\ell_{\perp}}. \quad (6d)$$

We can use the approximation $\ell_{\perp} \approx L_{\text{driv}}$, where L_{driv} is the driving length scale of the turbulence. The parallel Froude number Fr_{\parallel} is defined as

$$\text{Fr}_{\parallel} = \frac{v_{\perp}}{Nl_{\parallel}}, \quad \text{where} \quad (6e)$$

$$\ell_{\parallel} = 2\pi \frac{\int k_{\parallel}^{-1} E_{k_{\parallel}} dk_{\parallel}}{\int E_{k_{\parallel}} dk_{\parallel}}, \quad (6f)$$

with l_{\parallel} being the integral scale parallel to the direction of gravity and $E_{k_{\parallel}}$ is the velocity power spectrum parallel to the direction of \mathbf{g} . Notice that the transverse velocity (v_{\perp} , and not v_z) is used in the above expressions as v_z peaks at scales smaller than l_{\perp} . In this study, we use Fr_{\perp} to quantify the relative strength of stratification to turbulence³. The scale-dependent Froude numbers $\tilde{\text{Fr}}_{\perp}(\tilde{\ell}_{\perp})$ and $\tilde{\text{Fr}}_{\parallel}(\tilde{\ell}_{\parallel})$, for an eddy of size ($\tilde{\ell}_{\perp}$ and $\tilde{\ell}_{\parallel}$), and perpendicular velocity \tilde{v}_{\perp} are defined as

$$\tilde{\text{Fr}}_{\perp}(\tilde{\ell}_{\perp}) = \frac{\tilde{v}_{\perp}(\tilde{\ell}_{\perp})}{N\tilde{\ell}_{\perp}}, \quad (6g)$$

$$\tilde{\text{Fr}}_{\parallel}(\tilde{\ell}_{\parallel}) = \frac{\tilde{v}_{\perp}(\tilde{\ell}_{\perp})}{N\tilde{\ell}_{\parallel}}. \quad (6h)$$

$\text{Fr}_{\perp} \ll 1$ indicates strong stratification (in this regime, $\text{Fr}_{\parallel} \approx 1$, see [Billant & Chomaz 2001](#)) and $\text{Fr}_{\perp} \gg 1$ denotes weak stratification. Strongly stratified turbulence transitions into weakly stratified turbulence at the Ozmidov length scale ℓ_O , which is defined as the scale on which the relative strengths of buoyancy and turbulence terms become equal. Since $\tilde{\text{Fr}}_{\perp}(\ell_O) = 1$,

$$\ell_O = \sqrt{\epsilon_K / N^3}, \quad (6i)$$

where $\epsilon_K = v_{\perp}^3 / \ell_{\perp}$ is the kinetic energy transfer rate and is assumed to be a constant just as in conventional turbulence. For weak and moderately stratified turbulence ($\text{Fr}_{\perp} \gtrsim 1$), $\text{Fr}_{\perp} \approx (1/\text{Ri})^{0.5}$.

Similar to [MFS20](#), density, pressure and velocity are normalised to construct dimensionless variables, such that $\bar{\rho} = \rho / \langle \rho(z) \rangle$, $\bar{P} = P / \langle P(z) \rangle$ and $\mathcal{M} = \langle v / c_s \rangle_{\text{rms}}$, where $\langle \rho(z) \rangle$ and $\langle P(z) \rangle$ are the average density and pressure at a z - slice, respectively, v is the amplitude of velocity, and $c_s \equiv (\gamma \langle P \rangle / \langle \rho \rangle)^{1/2}$ is the

³ In [MFS20](#), we used the Richardson number (Ri) to quantify the strength of stratification, which is the ratio of buoyancy and turbulence terms in the momentum equation. For weakly and moderately stratified turbulence (the parameter regime that we scanned in [MFS20](#)), we used $\text{Ri} \approx N^2 L_{\text{driv}}^2 / v_{\perp}^2$. The assumption of isotropic eddies breaks down for strongly stratified turbulence, which is why we now parametrise the stratification in terms of the transverse Froude number (Fr_{\perp}).

local speed of sound. The potential energy per unit mass is defined as

$$E_{ub} = u_b^2 / 2 = \frac{P}{2\rho} \frac{\gamma \delta \bar{\rho}^2}{R_{PS}}, \quad (6j)$$

where $u_b = g\delta\bar{\rho}/N$ is the strength of density fluctuations expressed in velocity units, and

$$R_{PS} = H_P / H_S \quad (7)$$

is the ratio of pressure and entropy scale heights. The kinetic energy is defined as $E_u = \delta v^2 / 2$, where δv is the magnitude of the fluctuating velocity.

2.4 Numerical methods

We evolve the Euler equations ([1a](#) to [1c](#)) using the hydrodynamic version of the HLL5R Riemann solver ([Bouchut et al. 2007, 2010; Waagan et al. 2011](#)) in a modified version of the FLASH code ([Fryxell et al. 2000; Dubey et al. 2008](#)), version 4. Our setup is the same as in [MFS20](#) – we use a uniformly spaced 3D grid, with a box size $L_x = L_y = 1$ and $L_z = 1.5$, centred at $(0, 0, 0)$.

2.4.1 Boundary conditions

We use periodic boundary conditions for all variables (density, pressure and velocity) along the x and y directions. Along the z direction, we use reflective boundary conditions for velocity and Dirichlet boundary conditions for pressure and density with the guard cells filled according to eq. ([2a](#)) and ([2b](#)), respectively. In [MFS20](#), we used reflective boundary conditions along the z direction, which led to a hydrostatic instability at the z direction boundaries (due to an inverted pressure gradient at these boundaries). This instability was stronger for strongly stratified turbulence simulations and led to anomalous sound waves moving in the z direction, starting from the boundaries (also seen in [Shi & Zhang 2019](#), hereafter [SZ19](#)). The Dirichlet boundary conditions used here let us avoid this instability and allow us to extend our study to include the strongly stratified turbulence limit (down to $\text{Fr}_{\perp} \sim 0.05$).

We restrict our analyses to a cube of size 1 centred at $(0, 0, 0)$, with boundaries at $(\pm 0.5, \pm 0.5, \pm 0.5)$, to avoid any other anomalous effects near the z direction boundaries. We run our simulations with shallow density profile ($H_{\rho} > 1$) on grids with $256^2 \times 384$ resolution elements, and the simulations with steep density profile ($H_{\rho} \leq 1$) or simulations with high rms Mach number ($\mathcal{M} \approx 0.4$) on grids $512^2 \times 768$ resolution elements. We also run four strongly stratified simulations at resolution $1024^2 \times 1536$ for numerical convergence checks.

2.4.2 Turbulent forcing

We follow the same spectral forcing method as in [MFS20](#). We use the stochastic Ornstein-Uhlenbeck (OU) process to model the turbulent acceleration \mathbf{F} with a finite autocorrelation time scale t_{turb} ([Eswaran & Pope 1988; Schmidt et al. 2006; Federrath et al. 2010](#)). We inject power as a parabolic function of $|k|$, for $1 \leq |k| \leq 3$ (note that we have dropped the wavenumber unit $2\pi/L$). The power peaks at $|k|_{\text{inj}} = 2$, i.e., $L_{\text{driv}} = L/2$. For $k \geq 3$, turbulence develops self-consistently. We set $t_{\text{turb}} = L_{\text{driv}} / \sigma_v$, where σ_v is the standard deviation of the velocity on L_{driv} . Our driving is solenoidal (zero divergence). For further details of the forcing method, refer to section 2.7 of [MFS20](#) and section 2.1 in [Federrath et al. \(2010\)](#).

We also use the same window function, $w(z)$, on the acceleration field, as in [MFS20](#), such that \mathbf{F} decays to zero near the boundaries in the z direction, given by

$$w(z) = \begin{cases} 1, & \text{for } |z| < 0.625, \\ \exp(-|z| - 0.625)/0.125, & \text{for } |z| > 0.625. \end{cases}$$

Note that $w(z) = 1$ inside the analysis box ($|x|, |y|, |z| \leq 0.5$). So it only serves to exponentially decrease the acceleration amplitudes close to the z boundaries.

2.5 List of Simulation models

We have conducted 100 simulations, scanning Fr_\perp between 0.05–12.0, \mathcal{M} between 0.01–0.4 and R_{PS} between 0.33–2.33, covering the parameter range relevant for the stratified ICM. We have three input parameters (H_P , H_ρ and the acceleration field) that we vary in our various simulations to scan the range of interest in \mathcal{M} , Fr_\perp , and R_{PS} . The bin Mach number, \mathcal{M}_{bin} , indicates the rms Mach number that the acceleration field would produce in a homogeneous isotropic setup. We use these bins to separate our runs with different Mach numbers. The actual \mathcal{M} can be slightly different from \mathcal{M}_{bin} , especially in models with steep temperature profiles (H_ρ , $H_P \lesssim 0.25$), as c_s can vary by an order of magnitude with height. By definition, R_{PS} depends only on H_P/H_ρ (c.f., Equation (7)). Fr_\perp depends on all three input parameters, roughly $\text{Fr}_\perp \propto \mathcal{M}_{\text{bin}} H_P / \sqrt{R_{PS}}$ (as $u_\perp \propto \mathcal{M}_{\text{bin}}$ and $N^2 \propto 1/[H_P H_S]$).

In table 1, we provide a compressed list of the simulation models, grouped under their common \mathcal{M}_{bin} and R_{PS} . We indicate the range of H_ρ , the resolution, \mathcal{M} , Fr_\perp , and σ_s^2 (σ_s is the standard deviation of $s = \ln(\rho/\langle\rho\rangle)$ in the analysis box) for each of these groups. In table B1, we have expanded each grouping and list all of these parameters individually for each of the 100 simulations.

2.5.1 Dividing the analysis box into slabs

In order to take into account the variation in Fr_\perp and \mathcal{M} along z due to steep temperature profiles, and to maintain uniformity during post processing among all our simulations, we divide the the analysis data cube (see definition in section 2.4.1) into four slabs along the z direction ($-0.5 \leq z < -0.25$, $-0.25 \leq z < 0$, $0 \leq z < 0.25$ and $0.25 \leq z \leq 0.5$). This means that for each simulation, we have four sets of data-points (σ_s , $\sigma_{\ln(\bar{P})}$, \mathcal{M} , and Fr_\perp), corresponding to each of these four slabs.

In the presence of significant turbulent pressure (\propto local \mathcal{M}^2), comparable to the thermal pressure, our Dirichlet+reflective boundary conditions break hydrostatic equilibrium. This leads to fluctuations in the computational domain whose amplitude increases for steeper pressure profiles, since the thermal pressure is small at the $z = 0.75$ boundary. These fluctuations originate at the upper boundary, but they are confined close to the boundary itself, since strong stratification prevents them from travelling to lower z . Therefore, as a precaution, we ignore the upper two slabs and only use the lower two slabs in our analysis of simulations that have steep density or pressure profiles (H_P , $H_\rho < 0.25$).

All our simulations run for a total of 16 eddy turnover times ($t_{\text{eddy}} \approx t_{\text{turb}}$) on the driving length scale. The simulations reach a steady state between 3–6 t_{turb} . We analyse turbulence from 6 t_{turb} to 16 t_{turb} , for a total duration of 10 t_{turb} , for statistical averaging.

3 RESULTS AND DISCUSSION

Now we describe the results of our simulations and discuss their possible interpretations. We also compare our results against $\delta\bar{\rho}$ – $\delta\bar{P}$ – \mathcal{M} relations in other stratified turbulence simulations of the ICM.

3.1 Density and velocity projection maps

In fig. 1, we compare 6 representative simulation models (3 different models with high to low Froude number, from top to bottom, and 2 different Mach numbers, left versus right). Each panel shows the column density fluctuations $\delta\bar{\Sigma}_i = \int \bar{\rho} di - 1$, with the projected velocity field superimposed as vectors, where i denotes the line of sight (LOS) direction (the absolute column density $\Sigma_i = \int \rho di$ is shown in the insets to provide a sense of the strength of the stratification). We have chosen x as the LOS, which is perpendicular to the direction of stratification. For small density fluctuations ($\delta\bar{\rho} < 1$), the $\delta\bar{\Sigma}_x$ plots provide a sense of comparison (refer to section 3.2 of [MFS20](#)) to X-ray surface brightness fluctuations in [Zhuravleva et al. \(2014a\)](#), which have been used to reconstruct turbulent velocities of ICM gas.

For this figure, we have chosen 6 representative simulations, with two different \mathcal{M} and three different Fr_\perp , such that we roughly present the extremes of these two parameters. We have plotted them such that \mathcal{M} is approximately constant along a column, Fr_\perp is approximately constant along a row and R_{PS} is a constant for all.

For the Σ_x plots shown in the insets, we have used a separate log-scale colourbar for each row. The steepness of the Σ_x profile is inversely proportional to H_ρ . For these plots, $\text{Fr}_\perp \propto \mathcal{M} H_\rho$, as H_ρ decreases between the left and right panels, and also decreases from the top to the bottom panels. The column density fluctuations ($\delta\bar{\Sigma}_x$) increase with both \mathcal{M} and Fr_\perp , but are more sensitive to the changes in \mathcal{M} .

In the top and middle rows (weakly and moderately stratified turbulence), we observe that the eddies are roughly circular and hence the velocity field is roughly isotropic (similar to figure 3 of [MFS20](#)). However, for strongly stratified turbulence shown in the bottom row, the eddies become flatter in the z direction and turbulence forms layered stratified structures. We also observe the correlation between $\delta\bar{\Sigma}_x$ and v_z in the middle row, where upward velocity arrows ($v_z > 0$) are associated with regions where $\delta\bar{\Sigma}_x > 0$ (shown in red), and downward velocity arrows ($v_z < 0$) are associated with regions where $\delta\bar{\Sigma}_x < 0$ (shown in blue). This positive correlation implies that some of the kinetic energy is converted into buoyancy potential energy.

3.2 Velocity anisotropy

In homogeneous idealised turbulence, the velocity field is expected to be isotropic and to follow a nearly Gaussian distribution. However, external fields such as gravity (lower panel of fig. 4 in [MFS20](#); [SZ19](#)) and magnetic fields ([Federrath 2016](#); [Beattie et al. 2020](#)) can induce strong anisotropies in velocity fields. In our strongly stratified simulations, we expect the z component of velocity v_z to be the most affected by the strength of the stratification.

Understanding the variation in v_z as a function of stratification is of key significance to our study, since in [MFS20](#) we showed that the additional density fluctuations introduced by buoyancy effects ($\delta\bar{\rho}_{\text{buoy}}$) are correlated to v_z . We also derived a scaling relation for $\delta\bar{\rho}_{\text{buoy}}$, assuming the velocity field to be isotropic, i.e., $\langle v_z^2 \rangle \approx v^2/3$. However, this assumption breaks down for strongly stratified

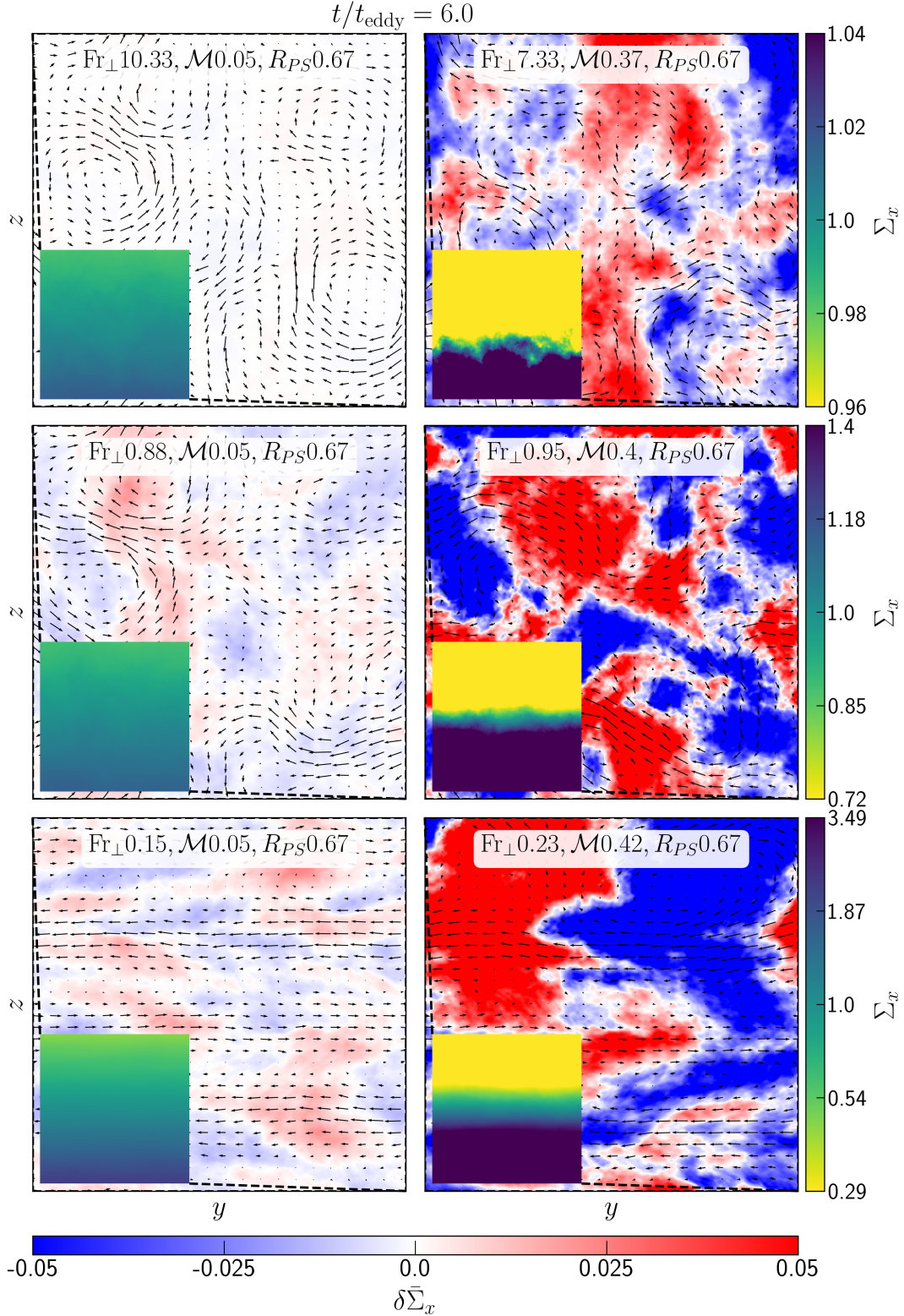


Figure 1. Normalised projected density fluctuations integrated over entire x - extent, $\delta \bar{\Sigma}_x$, with the x -integrated velocity field superimposed, for six representative simulations at $t = 6 t_{\text{eddy}}$. The insets show the projected profiles of density, Σ_x for the entire box, instead of the fluctuations. All of the 6 simulations shown have the same $R_{PS} = 0.67$ but different H_P, H_ρ to have roughly the same Fr_\perp in each row and the same \mathcal{M} in each column ($\approx 0.05, 0.4$). The Froude number in each row decreases from ~ 10 (top panels), to ~ 1 (middle panels), to ~ 0.2 (bottom panels). The colourbar for the $\delta \bar{\Sigma}_x$ panels (shown below the sub-panels) has a linear scale. Note that each row of the Σ_x insets has its own colourbar, which is in log scale. A movie of the time evolution of these representative simulations is available at this [youtube link](#).

Table 1. Simulation parameters for different runs

Label (1)	H_ρ range (2)	Resolution (3)	Actual \mathcal{M} range (4)	Fr_\perp range (5)	σ_s^2 range (6)
$M0.01R_{PS}0.67$	8.0—1.0	$512^2 \times 768$	0.0087—0.010	0.34—0.04	6.4×10^{-6} — 1.2×10^{-5}
$M0.05R_{PS}0.33$	17.3—0.55	$256^2 \times 384$ — $512^2 \times 768$	0.047—0.053	9.5—0.16	1.7×10^{-6} — 1.4×10^{-4}
$M0.05R_{PS}0.67$	21.3—0.28	$256^2 \times 384$ — $1024^2 \times 1536$	0.048—0.057	11.0—0.07	2.1×10^{-6} — 2.5×10^{-4}
$M0.05R_{PS}1.0$	21.9—0.2	$256^2 \times 384$ — $512^2 \times 768$	0.048—0.06	11.0—0.05	2.5×10^{-6} — 3.7×10^{-4}
$M0.05R_{PS}1.5$	17.8—0.2	$256^2 \times 384$ — $512^2 \times 768$	0.047—0.063	8.80—0.06	4.2×10^{-6} — 5.8×10^{-4}
$M0.05R_{PS}2.33$	20.0—0.2	$256^2 \times 384$ — $1024^2 \times 1536$	0.046—0.064	10.0—0.06	4.1×10^{-6} — 9.6×10^{-4}
$M0.10R_{PS}0.33$	8.7—0.273	$256^2 \times 384$ — $512^2 \times 768$	0.096—0.104	9.5—0.16	1.7×10^{-5} — 6.0×10^{-4}
$M0.10R_{PS}0.67$	9.6—0.22	$256^2 \times 384$ — $512^2 \times 768$	0.094—0.114	9.8—0.12	2.1×10^{-5} — 1.1×10^{-3}
$M0.10R_{PS}1.0$	11.2—0.22	$256^2 \times 384$ — $512^2 \times 768$	0.094—0.114	11.0—0.12	2.1×10^{-5} — 1.4×10^{-3}
$M0.10R_{PS}1.5$	10.6—0.22	$256^2 \times 384$ — $512^2 \times 768$	0.096—0.114	11.0—0.12	2.4×10^{-5} — 2.5×10^{-3}
$M0.10R_{PS}2.33$	10.0—0.2	$256^2 \times 384$ — $512^2 \times 768$	0.097—0.114	11.0—0.11	2.8×10^{-5} — 4.7×10^{-3}
$M0.25R_{PS}0.33$	3.5—0.125	$256^2 \times 384$ — $512^2 \times 768$	0.21—0.25	8.9—0.16	4.3×10^{-4} — 4.2×10^{-3}
$M0.25R_{PS}0.67$	6.4—0.12	$256^2 \times 384$ — $1024^2 \times 1536$	0.23—0.27	11.0—0.18	5.0×10^{-4} — 8.5×10^{-3}
$M0.25R_{PS}1.0$	7.0—0.10	$256^2 \times 384$ — $512^2 \times 768$	0.23—0.36	12.0—0.19	5.1×10^{-4} — 2.3×10^{-2}
$M0.25R_{PS}1.5$	6.4—0.10	$256^2 \times 384$ — $512^2 \times 768$	0.23—0.45	11.0—0.22	5.9×10^{-4} — 6.7×10^{-2}
$M0.25R_{PS}2.33$	6.0—0.1	$256^2 \times 384$ — $1024^2 \times 1536$	0.23—0.55	11.0—0.29	6.4×10^{-4} — 1.4×10^{-1}
$M0.40R_{PS}0.67$	1.8—0.15	$512^2 \times 768$	0.36—0.40	7.4—0.33	2.4×10^{-3} — 3.2×10^{-2}
$M0.40R_{PS}1.0$	1.75—0.17	$512^2 \times 768$	0.37—0.44	7.8—0.42	2.6×10^{-3} — 4.5×10^{-2}
$M0.40R_{PS}1.5$	1.4—0.14	$512^2 \times 768$	0.37—0.54	6.8—0.47	2.9×10^{-3} — 9.0×10^{-2}
$M0.40R_{PS}2.33$	1.3—0.12	$512^2 \times 768$	0.37—0.58	7.3—0.71	3.0×10^{-3} — 1.0×10^{-1}

Notes: Column 1 shows the simulation name. The numbers following ‘ \mathcal{M} ’ and ‘ R_{PS} ’ are the binned Mach number (M_{bin}) and the ratio of pressure to entropy scale heights H_P/H_S in the simulations, respectively. In columns 2 and 3 we list the H_ρ range and the resolution range. These parameters are defined in eqs. (2a) and (2b) and section 2.5. The default resolution of all the weak stratification runs ($H_\rho > 1$) is $256^2 \times 384$. The runs with stronger stratification ($H_\rho < 1$) or $M_{\text{bin}} = 0.4$ are run with $512^2 \times 768$ resolution elements. We also run four simulations at a resolution of $1024^2 \times 1536$, for convergence checks and four strongly stratified simulations at $\mathcal{M} = 0.01$ and resolution $512^2 \times 768$. Column 4 lists the actual rms \mathcal{M} range, which can be different from the targeted \mathcal{M} in strongly stratified simulations. In column 5, Fr_\perp refers to the mean perpendicular Froude number of the simulations (see equation 6d). Column 6 shows σ_s^2 , the standard deviation of $s = \ln \bar{\rho}$ squared. All quantities (\mathcal{M} , Fr_\perp , σ_s) were averaged over 10 turbulent turnover times, for $6 \leq t/t_{\text{turb}} \leq 16$. A more detailed version of this table, which lists each of the total of 96 simulations used here, is available in the appendix table B1.

turbulence ($\text{Fr}_\perp \ll 1$), since the velocity field becomes strongly anisotropic and motion is confined to layers perpendicular to the direction of gravity, as we see in the lower panels of fig. 1.

In order to investigate this further and understand the scaling of v_z with Fr_\perp , we show the ratio of $\langle v_z \rangle_{\text{rms}}$ to v_\perp (defined in eq. (6c)) in fig. 2. For weak stratification ($\text{Fr}_\perp \gg 1$), the velocity is roughly isotropic ($v_z/v_\perp \approx 1$)⁴, perpendicular and parallel velocities being roughly the same. As we move from right to left in fig. 2, in the moderately stratified turbulence regime ($\text{Fr}_\perp \approx 1$), the ratio starts decreasing slowly with decreasing Fr_\perp . This is expected, as more of the z direction kinetic energy gets converted into buoyancy potential energy with increasing strength of stratification. As we move further left in the plot to the strong stratification limit ($\text{Fr}_\perp \ll 1$), the ratio shows a sharp decrease with decreasing Fr_\perp , with $v_z/v_\perp \propto \text{Fr}_\perp^{0.7}$.

For strongly stratified turbulence, buoyancy dominates on large scales, for $\ell_O < \tilde{\ell} < L_{\text{driv}}$ (defined in eq. 6i), till the relative strengths of buoyancy and turbulence terms become equal. For $\tilde{\ell} < \ell_O$, the turbulence transitions to weakly stratified turbulence. Thus, unlike isotropic turbulence, v_z is set by $\tilde{v}_\parallel(\ell_O)$ instead of the integral scale velocity v_\parallel . For $\tilde{\ell} > \ell_O$, we may use the Boussinesq

approximation (changes in density are small relative to the mean density), for which eq. (1a) reduces to $\nabla \cdot \mathbf{v} = 0$. Then the ratio

$$\frac{\tilde{v}_\parallel(\tilde{\ell}_\perp)}{\tilde{v}_\perp(\tilde{\ell}_\perp)} \approx \frac{\tilde{\ell}_\parallel}{\tilde{\ell}_\perp} \approx \frac{\tilde{\text{Fr}}_\perp(\tilde{\ell}_\perp)}{\tilde{\text{Fr}}_\parallel(\tilde{\ell}_\perp)} \approx \tilde{\text{Fr}}_\perp(\tilde{\ell}_\perp) = \frac{\tilde{v}_\perp(\tilde{\ell}_\perp)}{N\tilde{\ell}_\perp}, \quad (8)$$

using eqs. (6g) and (6h), where we assume $\tilde{\text{Fr}}_\parallel \sim 1$ for strong stratification and that the vertical velocity fluctuations peak at the Ozmidov scale and not the driving scale. This gives us

$$\frac{v_z}{v_\perp} \approx \frac{\tilde{v}_\parallel(\ell_O)}{v_\perp} \approx \frac{\tilde{v}_\perp^2(\ell_O)}{N\ell_O v_\perp} = \frac{\epsilon_K^{2/3}}{\ell_O^{1/3} N v_\perp} = \text{Fr}_\perp^{0.5}, \quad (9)$$

using eqs. (6i) and (8) (see example 14.2 in Davidson 2013). We observe $v_z/v_\perp \propto \text{Fr}_\perp^{0.7 \pm 0.1}$ in our strongly stratified simulations, which roughly agrees with the theoretical prediction. Some deviations from the theoretical prediction may arise because the low-Froude simulations are not in the limit of $\text{Fr}_\perp \ll 1$, but around $\text{Fr}_\perp \sim 0.1$.

3.3 Density and pressure fluctuations

In this subsection, we discuss the variation of density and pressure fluctuations as a function of our simulation parameters - \mathcal{M} , Fr_\perp

⁴ From here on, we denote $\langle v_z \rangle_{\text{rms}}$ as v_z .

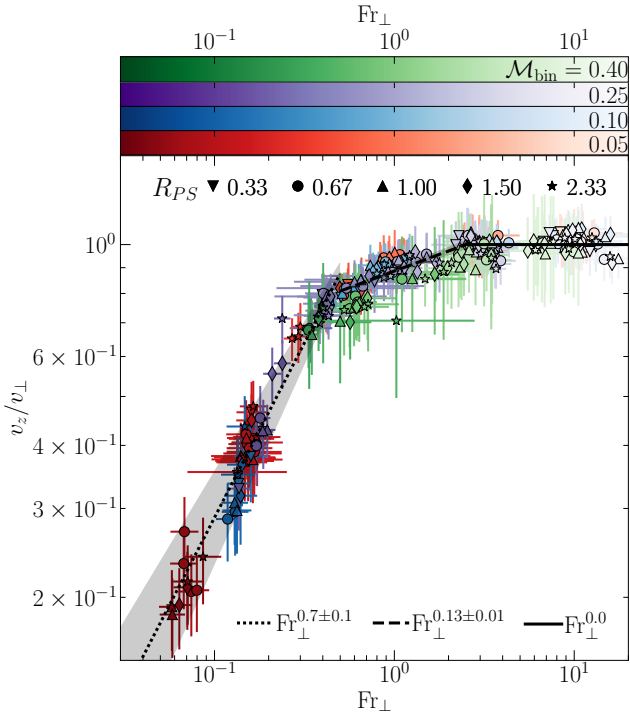


Figure 2. The ratio between v_z and v_{\perp} versus Fr_{\perp} , where v_z and v_{\perp} are the rms values of one-component velocities perpendicular and parallel to the direction of stratification, respectively, averaged over slabs in the z direction (see subsection 2.5.1). Colours red, blue, purple and green indicate the M_{bin} of the runs. Different shades of these colours indicate the value of Fr_{\perp} , as shown in the colourbars. The different symbols indicate different values of the ratio $R_{PS} = H_P/H_S$. The dotted, dashed, and solid lines indicate fits in the low to high Fr_{\perp} regime. The shaded region around the fits shows the 1σ error margins in the fitting parameters. We see significant anisotropies arising in the turbulence, for strong stratification ($Fr_{\perp} \lesssim 0.5$).

and R_{PS} . The scaling relations between these quantities are important for obtaining ICM gas velocity estimates from X-ray and SZ observations. The X-ray surface brightness fluctuations and SZ effect fluctuations are used to calculate the amplitude of density and pressure fluctuations, respectively, which are further used to calculate velocity fluctuations using these relations (Zhuravleva et al. 2013, 2014b; Khatri & Gaspari 2016).

3.3.1 Density and pressure fluctuations as a function of \mathcal{M}

In fig. 3, we show the density and pressure fluctuations squared (σ_s^2 and $\sigma_{\ln \bar{P}}^2$) versus \mathcal{M} for all our simulations. We also present approximate fits based on the scaling relations that we propose in the next section 3.3.2. Clearly, σ_s^2 increases with increasing \mathcal{M} , stratification strength (decreasing Fr_{\perp}) and R_{PS} . In comparison, $\sigma_{\ln \bar{P}}^2$ only increases with \mathcal{M} and is independent of Fr_{\perp} and R_{PS} .

As we discussed in section 3.5 of MFS20, the density fluctuations are comprised of two components, which can be written as the sum of an un-stratified and a stratified turbulence component:

$$\delta \bar{\rho}^2 = \delta \bar{\rho}_{\text{turb}}^2 + \delta \bar{\rho}_{\text{buoy}}^2, \quad (10)$$

where $\delta \bar{\rho}_{\text{turb}}^2$ scales as $b^2 \mathcal{M}^4$ (Mohapatra & Sharma 2019; MFS20), and b is the turbulence driving parameter (Federrath et al. 2008). The parameter $b = 1/3$ for solenoidal turbulence, as we use for the present set of simulations. Our fits in fig. 3 show this dependence on \mathcal{M} for $Fr_{\text{fit}} \gg 1$ (light bronze coloured fits). We also showed

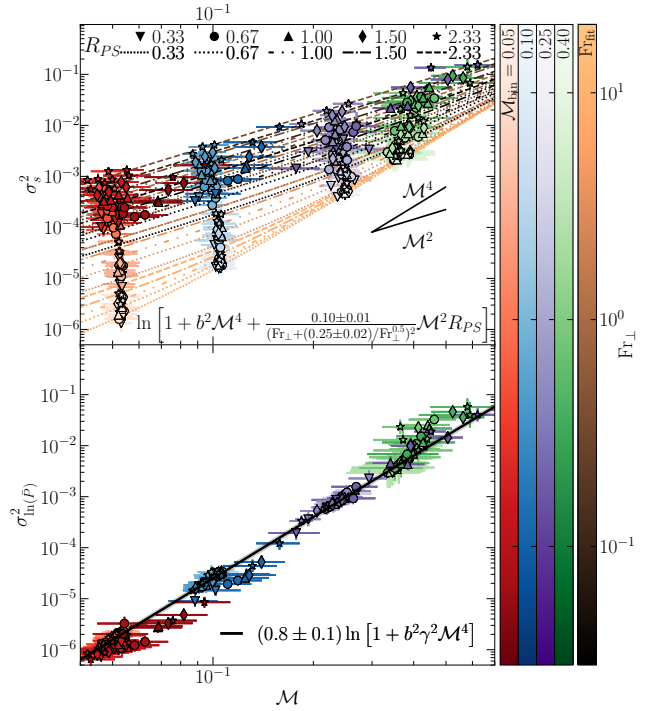


Figure 3. The density and pressure fluctuations (σ_s^2 ; upper panel and $\sigma_{\ln \bar{P}}^2$; lower panel) versus the rms Mach number (\mathcal{M}) for all our simulations. The rightmost colourbar indicates the value of Fr_{\perp} used for plotting the different fits in the upper panel. The different line styles indicate the value of the ratio $R_{PS} = H_P/H_S$ used for the different fits in the upper panel. The shades on different symbols correspond to the different Froude numbers. Density fluctuations are smaller for a larger Fr_{\perp} (weaker stratification). The respective fitting functions (section 3.3.2) for the upper and lower panels are indicated in the bottom right corner of each panel. For reference, we have also shown sample \mathcal{M}^2 and \mathcal{M}^4 scaling in the upper panel.

that $\delta \bar{\rho}_{\text{turb}}$ corresponds to adiabatic density fluctuations, so the corresponding pressure fluctuations $\delta \bar{P}^2$ scale as $\gamma^2 \delta \bar{\rho}_{\text{turb}}^2 \propto \mathcal{M}^4$ for $Fr_{\perp} \gg 1$. The $\delta \bar{\rho}_{\text{turb}}^2$ component of density fluctuations dominates for weakly stratified turbulence or at large \mathcal{M} .

For moderate stratification ($Fr_{\perp} \sim 1$) or low \mathcal{M} turbulence, the $\delta \bar{\rho}_{\text{buoy}}$ term dominates, but it corresponds to the isobaric motions of isotropic gas parcels, which have zero contribution to the net pressure fluctuations. Hence $\delta \bar{P}$ still scales as $\gamma \delta \bar{\rho}_{\text{turb}}$ and shows a \mathcal{M}^4 variation throughout as seen in the lower panel of fig. 3. This scaling seems to hold even in the strongly stratified turbulence limit, which means that the nature of $\delta \bar{\rho}_{\text{buoy}}$ is isobaric even for $Fr \ll 1$. This behaviour is expected, since a rising/falling parcel of gas with subsonic velocity is always in pressure equilibrium with its immediate surroundings (such that $\delta \bar{P}_{\text{buoy}} = 0$). Thus, the expression for logarithmic pressure fluctuations becomes

$$\sigma_{\ln \bar{P}}^2 = \ln \left[1 + b^2 \gamma^2 \mathcal{M}^4 \right]. \quad (11)$$

In the lower panel of fig. 3, we fit the data to eq. (11) using the fitting tool LMfit (Newville et al. 2016). The results are in good agreement with our expectations.

In MFS20, we also showed that $\delta \bar{\rho}_{\text{buoy}}^2$ increases with \mathcal{M} as approximately \mathcal{M}^2 , for constant $Fr_{\perp} \gtrsim 1$ (or $Ri \lesssim 1$). The motions in the z direction associated with $\delta \bar{\rho}_{\text{buoy}}$ are strongly constrained for $Fr_{\perp} \ll 1$ and because of the large energy cost, BV oscillations (with small displacement in the z direction) dominate over turbulence in

the vertical direction. But the scaling with \mathcal{M} still holds in this limit, as is seen in the dark bronze fits in the upper panel of fig. 3.

3.3.2 Density & pressure fluctuations as a function of Fr_\perp and R_{PS}

In this subsection, we discuss the scaling of density and pressure fluctuations with the stratification parameters Fr_\perp and R_{PS} . We know that the $\delta\bar{\rho}_{\text{turb}}^2$ and $\delta\bar{\rho}_{\text{buoy}}^2$ terms scale as \mathcal{M}^4 and \mathcal{M}^2 , respectively. In order to make comparisons between different Fr_\perp and R_{PS} easier, we normalise σ_s^2 and $\sigma_{\ln \bar{P}}^2$ to $\sigma_{s,\text{bin}}^2$ and $\sigma_{\ln \bar{P},\text{bin}}^2$, respectively, given by

$$\sigma_{s,\text{bin}}^2 = \ln \left[1 + b^2 \mathcal{M}_{\text{bin}}^4 + \frac{\mathcal{M}_{\text{bin}}^2}{\mathcal{M}^2} \left(\exp\{\sigma_s^2\} - 1 - b^2 \mathcal{M}^4 \right) \right], \quad (12a)$$

$$\sigma_{\ln \bar{P},\text{bin}}^2 = \ln \left[1 + \frac{\mathcal{M}_{\text{bin}}^4}{\mathcal{M}^4} \left(\exp\{\sigma_{\ln \bar{P}}^2\} - 1 \right) \right]. \quad (12b)$$

This way, the runs with different \mathcal{M} are scaled to the same \mathcal{M}_{bin} . We described \mathcal{M}_{bin} in section 2.5 and $\mathcal{M}_{\text{bin}} \approx \mathcal{M}$ for shallow initial density and pressure profiles ($H_P, H_\rho \gtrsim 1$). We take four different values of \mathcal{M}_{bin} , namely $\mathcal{M}_{\text{bin}} = 0.05, 0.10, 0.25$, and 0.40 . We show $\sigma_{s,\text{bin}}^2$ and $\sigma_{\ln \bar{P},\text{bin}}^2$ vs Fr_\perp in fig. 4.

As we move from right to left in this plot (increasing stratification and decreasing Fr_\perp), $\sigma_{s,\text{bin}}^2$ increases for $\text{Fr}_\perp \gtrsim 0.5$. It reaches a peak around $\text{Fr}_\perp \approx 0.5$ and starts decreasing for smaller Fr_\perp . For $\text{Fr}_\perp \lesssim 1$, $\sigma_{s,\text{bin}}^2$ increases with R_{PS} , but this dependence is weaker as compared to that on Fr_\perp . For a constant \mathcal{M}_{bin} , $\sigma_{\ln \bar{P},\text{bin}}^2$ stays constant with both Fr_\perp and R_{PS} , as expected from eq. (11).

All the variation in $\sigma_{s,\text{bin}}^2$ can be attributed to the dependence of $\delta\bar{\rho}_{\text{buoy}}^2$ on these stratification parameters, since $\delta\bar{\rho}_{\text{turb}}^2$ depends only on \mathcal{M} . The $\delta\bar{\rho}_{\text{buoy}}^2$ component is correlated with the rms displacement in the z direction $\langle \delta z^2 \rangle$ and is given by

$$\delta\bar{\rho}_{\text{buoy}}^2 = \frac{N^4}{g^2} \langle \delta z^2 \rangle. \quad (13a)$$

In the weak and moderately stratified turbulence limit ($\text{Fr}_\perp \gtrsim 1$), we simplify this expression further and showed in MFS20 that

$$\delta\bar{\rho}_{\text{buoy}}^2 \approx \zeta^2 \mathcal{M}^2 \text{Ri} R_{PS} \approx \zeta^2 \frac{\mathcal{M}^2 R_{PS}}{\text{Fr}_\perp^2}, \quad (13b)$$

where ζ^2 is a fitting parameter. However, this simplification involved assuming the velocity field to be roughly isotropic, which is true for $\text{Fr}_\perp \gtrsim 0.5$ (see fig. 2), not for strongly stratified turbulence. In the limit of strongly stratified turbulence ($\text{Fr}_\perp \ll 1$), the z direction motions are heavily suppressed by buoyancy and the velocity field is no longer isotropic, as we showed in section 3.2. In this limit,

$$\begin{aligned} \delta\bar{\rho}_{\text{buoy}}^2 &\approx \frac{N^4}{g^2} \langle \delta z^2 \rangle \approx \frac{N^4}{g^2} \zeta'^2 \frac{v_z^2}{N^2} \\ &\approx \zeta'^2 \mathcal{M}^2 \text{Fr}_\perp R_{PS}, \end{aligned} \quad (13c)$$

using eqs. (3a), (6a) and (9). Interpolating between the two asymptotic expressions for $\delta\bar{\rho}_{\text{buoy}}^2$ in eq. (13b) and eq. (13c), we get

$$\delta\bar{\rho}_{\text{buoy}}^2 = \frac{\zeta_1^2 \mathcal{M}^2 R_{PS}}{(\text{Fr}_\perp + \zeta_2 / \sqrt{\text{Fr}_\perp})^2}, \quad (13d)$$

where ζ_1 and ζ_2 are fitting parameters. The combined expression

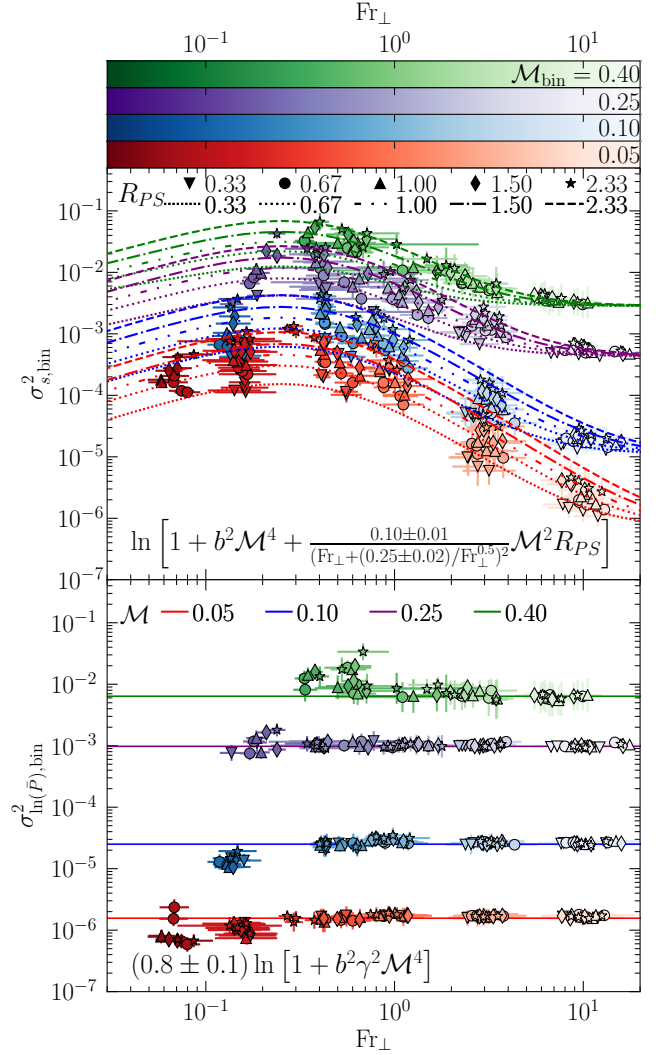


Figure 4. The density and pressure fluctuations ($\sigma_{s,\text{bin}}^2$; upper panel and $\sigma_{\ln \bar{P},\text{bin}}^2$; lower panel) versus the transverse Froude number (Fr_\perp) for all our simulations. The symbol shape corresponds to R_{PS} and the shade indicates the Mach number. The different line styles indicate the value of the ratio R_{PS} used for our different fits in the upper panel. The fits are given in individual panels.

for the net density fluctuations is then given by

$$\delta\bar{\rho}^2 = b^2 \mathcal{M}^4 + \frac{\zeta_1^2 \mathcal{M}^2 R_{PS}}{(\text{Fr}_\perp + \zeta_2 / \sqrt{\text{Fr}_\perp})^2} \quad \text{and} \quad (13e)$$

$$\sigma_s^2 = \ln \left[1 + b^2 \mathcal{M}^4 + \frac{\zeta_1^2 \mathcal{M}^2 R_{PS}}{(\text{Fr}_\perp + \zeta_2 / \sqrt{\text{Fr}_\perp})^2} \right]. \quad (13f)$$

Here we substituted $\sigma_s^2 = \ln [1 + \sigma_\rho^2]$. This is valid for log-normal distributions of $\bar{\rho}$ but it also holds approximately for non-log-normal distributions with small σ_ρ^2 (see Appendix 7).

Thus, we find that introducing stratification has two main effects. For $\text{Fr}_\perp \gtrsim 0.5$, due to the existing density gradient, the turbulent motions in the z direction produce higher density fluctuations. This happens simply because when a gas parcel moves along the z direction, it only attains pressure equilibrium at that height, but still has a density contrast with respect to its surroundings. On assuming isotropic gas velocities, which is roughly valid for $\text{Fr} \gtrsim 0.5$ (see

fig. 2), we obtain $\delta\bar{\rho}_{\text{buoy}}^2 = \zeta^2 \mathcal{M}^2 R_{PS} / \text{Fr}_{\perp}^2$ (eq. 13b). However, on further increasing the stratification ($\text{Fr}_{\perp} \lesssim 0.5$), the turbulence becomes anisotropic as gas motions along the z direction are suppressed, with the kinetic energy along the z direction being converted into buoyancy potential energy. The turbulent eddies flatten along the z direction and become pancake-like (see lower panels of fig. 1). In this limit, the motion along the z direction is best described by BV oscillations. The amplitude of these oscillations is proportional to v_z , which decreases with decreasing Fr_{\perp} for constant \mathcal{M} (see fig. 6). Substituting the Fr_{\perp} dependence of the ratio v_z/v_{\perp} , we obtain $\delta\bar{\rho}_{\text{buoy}}^2 = \zeta'^2 \mathcal{M}^2 R_{PS} \text{Fr}_{\perp}$ (eq. 13c). The general expression for the dependence of $\delta\bar{\rho}_{\text{buoy}}^2$ (eq. 13d) is thus an interpolation between these two forms.

For even stronger stratification ($\text{Fr}_{\perp} \lesssim 0.001$), we expect the amplitude of $\delta\bar{\rho}_{\text{buoy}}^2$ to decrease below $\delta\bar{\rho}_{\text{turb}}^2$, and the net density fluctuations would again be given by $\delta\bar{\rho}^2 \sim b^2 \mathcal{M}^4$, similar to the unstratified subsonic turbulence scaling. One can interpret this limit as 2D subsonic turbulence, with \mathcal{M} representing the 2D Mach number, since $v_z \ll v_{\perp}$.

3.3.3 Obtaining the fitting parameters

Here we derive the fitting parameters ζ_1 and ζ_2 , such that they describe the variation in density fluctuations for all of our 96 simulations simultaneously. We use the fitting tool LMfit with eq. (13f) as the fitting function, \mathcal{M} , Fr_{\perp} and R_{PS} as independent variables, and σ_s^2 as the dependent variable. We obtain $\zeta_1^2 = 0.10 \pm 0.01$ and $\zeta_2 = 0.25 \pm 0.02$.

In order to present all our data and the fitting function together, we scale all density and pressure fluctuations to $\mathcal{M}_{\text{scaled}} = 0.25$ and $R_{PS} = 2.33$. These are the same parameter values we used in all simulations of MFS20 and hence they provide a direct comparison between both of our studies. We construct two new scaled quantities, given by

$$\sigma_{s,\text{scaled}}^2 = \ln \left[1 + b^2 (0.25)^4 + \left(\frac{0.25}{\mathcal{M}} \right)^2 \frac{2.33}{R_{PS}} \right] \times \left(\exp\{\sigma_s^2\} - 1 - b^2 \mathcal{M}^4 \right) \quad \text{and} \quad (14a)$$

$$\sigma_{\ln \bar{P},\text{scaled}}^2 = \ln \left[1 + \left(\frac{0.25}{\mathcal{M}} \right)^4 \left(\exp\{\sigma_{\ln \bar{P}}^2\} - 1 \right) \right]. \quad (14b)$$

In fig. 5, we show these two quantities as a function of Fr_{\perp} . We also show the fitting function eq. (13f) for $\mathcal{M} = 0.25$ and $R_{PS} = 2.33$. Thus, our scaling relation for σ_s^2 works well for the entire range of parameter space we have scanned using the 96 simulations. The value of $\sigma_{\ln \bar{P},\text{scaled}}^2$ is roughly constant, as expected from eq. (11). We expect the variation to be mostly due to two reasons both leading to inaccurate estimates of \mathcal{M} , and these variations are amplified in the plot since $\sigma_{\ln \bar{P},\text{scaled}}^2 \propto \mathcal{M}^4$. Firstly, the box heats up in larger \mathcal{M}_{bin} simulations (especially $\mathcal{M}_{\text{bin}} = 0.25$ and 0.4), which leads to an increased speed of sound and a decreased Mach number. Secondly, due to the steep temperature profiles for simulations with $H_P, H_{\rho} < 0.2$, ($H_P \neq H_{\rho}$), the speed of sound significantly varies along the z direction, whereas we drive an isotropic velocity field. This leads to a strong variation in \mathcal{M} along the z direction, which may cause the differences from the scaling relations for $\text{Fr}_{\perp} \lesssim 0.5$.

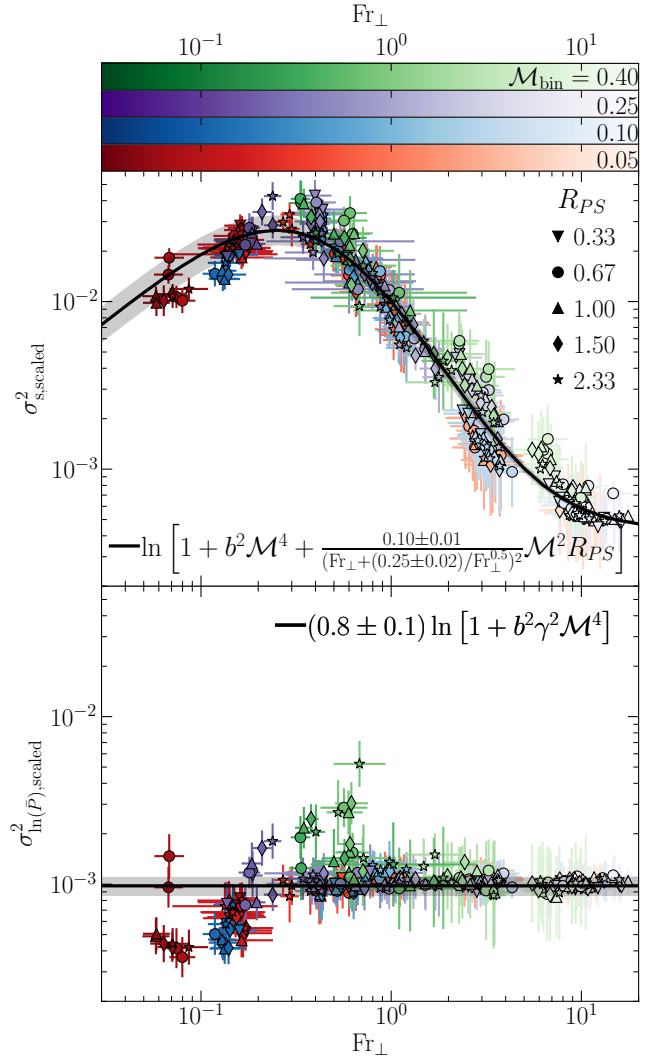


Figure 5. The density ($\sigma_{s,\text{scaled}}^2$; upper panel) and pressure fluctuations ($\sigma_{\ln \bar{P},\text{scaled}}^2$; lower panel), scaled such that they collapse on to a single line as a function of Fr_{\perp} all our simulations. The symbol shape corresponds to R_{PS} and the colours indicate the Mach number. The fits are shown in the respective panels. The shaded region around the fits shows the 1σ error margins in the fitting parameters.

3.3.4 Pressure fluctuations and the SZ effect

In this subsection we discuss the importance of pressure fluctuations for estimating turbulent gas velocities in the ICM. In the previous subsections, we showed that density fluctuations are sensitive to the parameters Fr_{\perp} and R_{PS} , whereas pressure fluctuations depend only on \mathcal{M} . We found that the relation $\sigma_{\bar{P}}^2 = b^2 \gamma^2 \mathcal{M}^4$ describes all our simulations very well (see lower panels of fig. 3 and fig. 5). This happens because the stratified turbulence component of density fluctuations is isobaric (see figure 8 of MFS20). In figure 14 of Mohapatra & Sharma (2019), we also showed that pressure fluctuations do not significantly depend on whether radiative cooling is included or not. While density fluctuations are sensitive to the thermodynamic and stratification parameters, pressure fluctuations are independent of these. Thus, compared to density fluctuations, we expect pressure fluctuations to provide a robust estimate of turbulent velocities.

Hot electrons in the ICM, on average, up-scatter the cosmic

Table 2. Simulation parameters for the $M = 0.01$, $\text{Fr}_\perp < 0.4$ runs

Label (1)	H_ρ (2)	M (3)	σ_s^2 (4)	$\sigma_{\log \bar{P}}^2$ (5)
Fr0.34M0.01R _{PS} 0.67	8.0	$(8.7 \pm 0.3) \times 10^{-3}$	$1.2^{+0.2}_{-0.2} \times 10^{-5}$	$1.4^{+0.3}_{-0.4} \times 10^{-9}$
Fr0.18M0.01R _{PS} 0.67	4.0	$(8.9 \pm 0.4) \times 10^{-3}$	$1.1^{+0.1}_{-0.2} \times 10^{-5}$	$1.4^{+0.2}_{-0.3} \times 10^{-9}$
Fr0.09M0.01R _{PS} 0.67	2.0	$(9.9 \pm 0.8) \times 10^{-3}$	$7.0^{+1.2}_{-1.5} \times 10^{-6}$	$1.6^{+0.4}_{-0.6} \times 10^{-9}$
Fr0.04M0.01R _{PS} 0.67	1.0	$(1.0 \pm 0.1) \times 10^{-2}$	$6.4^{+1.1}_{-1.4} \times 10^{-6}$	$2.5^{+0.6}_{-0.8} \times 10^{-9}$

Notes: All these simulations have grid resolution $512^2 \times 768$. The columns (2) - (5) have their usual meanings. For these runs, $H_P/H_\rho = 1$.

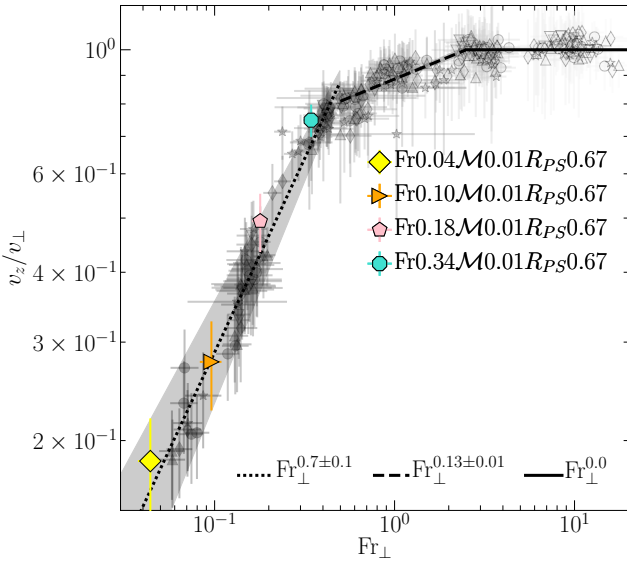


Figure 6. The ratio between v_z and v_\perp versus Fr_\perp for our simulations with $M \approx 0.01$, $R_{PS} = 0.67$, and $\text{Fr}_\perp \lesssim 0.4$. We also show our data points from fig. 2 in grey. The low- M data follow the $\text{Fr}_\perp^{0.7}$ scaling for $\text{Fr}_\perp \lesssim 0.4$.

microwave background (CMB) photons through inverse Compton scattering, and the change in the CMB brightness temperature is proportional to the ICM electron pressure integrated along the line of sight. This effect is known as the thermal Sunyaev-Zeldovich (tSZ) effect (see [Mroczkowski et al. 2019](#), for a review). Although it is possible to recover turbulent gas velocities from the resolved observations of the tSZ effect ([Khatri & Gaspari 2016](#)), the present observations suffer from a lack of angular resolution (e.g., up to a few 100 kpc for the Coma cluster). The tSZ observations also suffer from projection effects (more than X-ray surface brightness which is proportional to ρ^2), which makes the measured pressure fluctuations even smoother than the density fluctuations. Many of these limitations are expected to be addressed by future facilities (see section 6.2 of [Mroczkowski et al. 2019](#)). The relative robustness of the relation between pressure fluctuations and turbulent velocities (unlike density fluctuations which depend on stratification and thermodynamic parameters) provides a strong motivation for high angular resolution SZ observations.

3.3.5 Testing the scaling relation at lower M and $\text{Fr}_\perp \ll 1$

In this subsection we test the scaling of the velocity ratio, density and pressure fluctuations with Fr_\perp through 4 simulations at $M \approx 0.01$, $R_{PS} = 0.67$ and $\text{Fr}_\perp \lesssim 0.4$. See table 2 for the simulation parameters. Since these simulations have $H_P = H_\rho$, the sound speed is

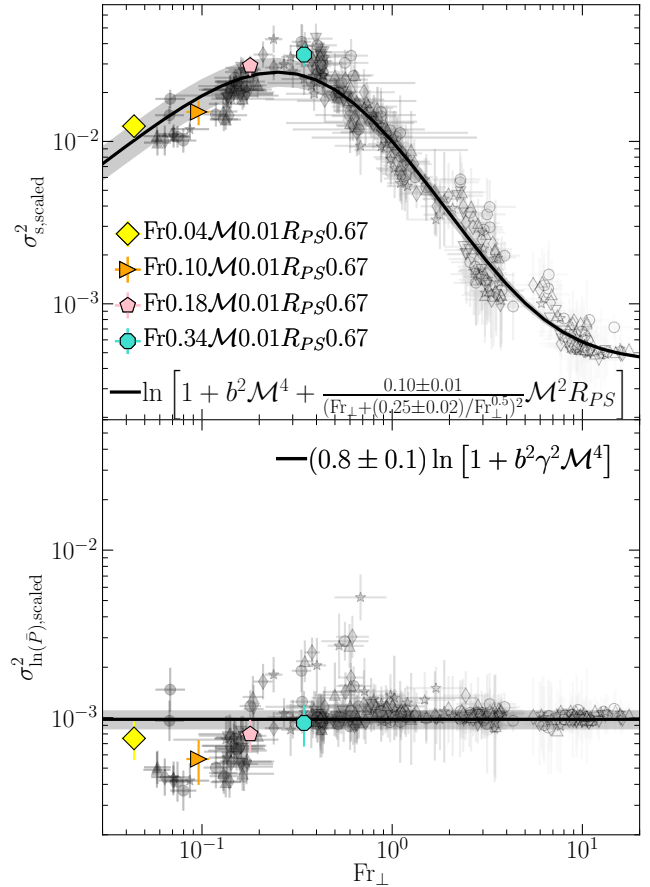


Figure 7. The scaled density ($\sigma_{s,\text{scaled}}^2$; upper panel) and pressure fluctuations ($\sigma_{\log \bar{P},\text{scaled}}^2$; lower panel) for our simulations with $M \approx 0.01$, $R_{PS} = 0.67$, and $\text{Fr}_\perp \lesssim 0.4$. We also show our data points from fig. 5 in grey. The low- M data follows our proposed scaling relation for both density and pressure fluctuations.

uniform throughout the domain and the turbulent pressure is negligible compared to the thermal pressure (turbulent pressure $\sim 10^{-4}$ thermal pressure). Since $H_P, H_\rho > 1.0$, the density and pressure gradients are not very steep. Thus, these simulations do not suffer from fluctuations near the boundaries mentioned in sections 2.4.1 and 2.5.1.

In fig. 6 we show the ratio between v_z and v_\perp for these simulations. The ratio follows the $\text{Fr}_\perp^{0.7}$ scaling. In fig. 7 we show $\sigma_{s,\text{scaled}}^2$ and $\sigma_{\ln(\bar{P}),\text{scaled}}^2$, and we find that they also follow the scaling relation in the low- Fr_\perp regime— $\sigma_{s,\text{scaled}}^2$ decreases with decreasing Fr_\perp and $\sigma_{\ln(\bar{P}),\text{scaled}}^2$ is independent of Fr_\perp .

3.3.6 Comparing the density scaling relation with other studies

In this subsection, we test our scaling relation against data from [SZ19](#), who study decaying turbulence in a stratified medium, using a setup similar to ours. We have received the simulation snapshots from [Shi & Zhang](#) and applied our analysis methods to calculate σ_s^2

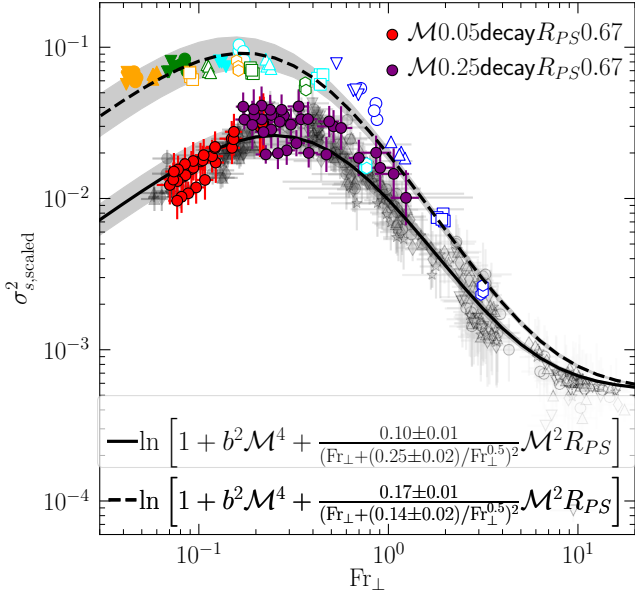


Figure 8. The scaled density fluctuations ($\sigma_{s,\text{scaled}}^2$) vs Fr_\perp with the coloured (cyan, green and orange) datapoints taken from SZ19 and scaled (see the main text). We follow the same colour and marker scheme as in figure 8 of SZ19, where different colours represent different values of N (which correspond to simulations with different levels of stratification). The open symbols are for $t \leq 2/N$ and the filled symbols are for $t > 2/N$. We show our data points from the top panel of fig. 5 in grey. We have also plotted data points from our turbulence decay simulations in red and purple. The dashed line shows the best fit to SZ19’s data and the solid line shows the best fit to our data. There seems to be a small scaling discrepancy which becomes larger at smaller Fr_\perp . We discuss more about this discrepancy and its possible sources in the main text.

and Fr_\perp .⁵ We scale these quantities to $\sigma_{s,\text{scaled}}^2$ with $\mathcal{M} = 0.25$ and $R_{PS} = 2.33$, using eq. (14a).

In fig. 8, we show $\sigma_{s,\text{scaled}}^2$ as a function of Fr_\perp , using the same colour scheme (cyan, green and orange) and markers as figure 8 in SZ19. We have greyed out our data points in the background. SZ19 study decaying turbulence, and therefore all variables are time (t) dependent in their study. The open symbols in fig. 8 are for $t \leq 2/N$ and the filled symbols are for $t > 2/N$. The dashed line is the best fit to the scaled SZ19 data and the solid line is the best fit to our data.

We find that at high Fr_\perp , $\sigma_{s,\text{scaled}}^2$ for SZ19’s data shows a similar dependence on Fr_\perp as our scaling relation predicts. However, the exact dependence of $\sigma_{s,\text{scaled}}^2$ on Fr_\perp is somewhat different, i.e., we see that $\sigma_{s,\text{scaled}}^2$ is higher by almost a factor of 2–4 for $\text{Fr}_\perp \lesssim 0.5$ becomes independent of Fr_\perp for $\text{Fr}_\perp \lesssim 0.3$. We find that the fitting parameters ζ_1^2 and ζ_2 (see eq. (13f)) take the values 0.17 ± 0.01 and 0.14 ± 0.02 respectively.

The open data points for $t \leq 2/N$ in SZ19 correspond to the moderate-weakly stratified turbulence regime ($\text{Fr}_\perp \gtrsim 0.5$). In this limit,

$$\delta\bar{\rho}^2 \approx \delta\bar{\rho}_{\text{buoy}}^2 \propto \mathcal{M}^2 / \text{Fr}_\perp^2 = N^2 \ell_\perp^2 / c_s^2. \quad (15)$$

For a given stratification profile (fixed H_P , H_ρ and corresponding

⁵ Our values of Fr_\perp for SZ19 differ by a factor of 2π . This results from the slightly different definitions of the integral scale l_\perp (see equation 3 in SZ19), where 2π is the conversion factor from wavenumber space to real space.

N) and $t \leq 2/N$, $\delta\bar{\rho}^2$ is independent of \mathcal{M} , as seen in figure 8 of SZ19. This has significant implications for observational studies, which infer turbulent velocities from surface brightness fluctuations, which are in turn caused by density fluctuations. For $t > 2/N$, $\text{Fr}_\perp \lesssim 0.5$, where the σ_s^2 dependence on Fr_\perp is weak near the peak of the proposed scaling relation and hence $\delta\bar{\rho}^2 \propto \mathcal{M}^2$.

In order to directly compare against SZ19, we conduct two sets of turbulence decay simulations with $\mathcal{M}_{\text{bin}} = 0.05$ and 0.25 , $H_P = H_\rho = 1.0$ with grid resolution $512^2 \times 768$. Once turbulence reaches a roughly steady state (after $\approx 3t_{\text{eddy}}$), we switch off external driving. We simulate five statistically similar instances of decaying turbulence by changing the random number seed for the turbulent driving.

We calculate the average value of σ_s^2 over time intervals of $2t_{\text{eddy}}$ in the decay phase. We further average these values across the five runs. The red and purple circles in fig. 8 represent $\sigma_{s,\text{scaled}}^2$ for these decaying turbulence simulations. Both the purple and red data points agree with our proposed scaling relation. Unlike SZ19’s data, for $\text{Fr}_\perp \lesssim 0.3$, $\sigma_{s,\text{scaled}}^2$ in decaying turbulence simulations decreases with decreasing Fr_\perp , similar to our steady-state turbulence runs.

The differences in the values of $\sigma_{s,\text{scaled}}^2$ at low Fr_\perp may arise due to the spurious sound waves as discussed in section 2.4.1. Due to the reflective boundary conditions along the z direction, they can form standing waves in pressure (X. Shi, private communication). If the amplitude of density fluctuations due to the standing waves is comparable to $\delta\bar{\rho}_{\text{buoy}}$, then the net density fluctuations would not show a decrease at the low Fr_\perp limit. Our turbulence decay simulations do not suffer from this because of the new Dirichlet boundary conditions that we apply to the density and pressure. These simulations are at low rms Mach number and use an initially isothermal stratification profile ($H_P = H_\rho = 1.0$). Hence they also do not suffer from the numerical fluctuations at the upper boundary discussed in section 2.5.1.

3.4 Density fluctuations versus velocity power spectra in strongly stratified turbulence

In the previous subsections we have investigated the scaling of rms density fluctuations with the rms Mach number, Fr_\perp , and R_{PS} . Another quantity relevant for observations is the amplitude and spectral scaling of density fluctuations and velocity power spectra. This is because turbulent velocities are more difficult to measure directly in observations, and often the surface brightness fluctuations are used to infer properties of the turbulence (Zhuravleva et al. 2014a, 2015, 2018 and Simionescu et al. 2019 for a review).

The ratio between Fourier one-component density fluctuation amplitudes $\delta\bar{\rho}_k$ and Fourier one-component velocity amplitudes $v_{1,k}$ is denoted by η_k and it is related to the density fluctuations and velocity power spectra by

$$\eta_k^2 = (\delta\bar{\rho}_k)^2 / (v_{1,k}/c_s)^2 \approx 3P(\delta\bar{\rho}_k) / P(\mathcal{M}_k), \quad (16)$$

where $P(\delta\bar{\rho}_k)$ and $P(\mathcal{M}_k)$ are the density fluctuations and velocity power spectra. Density and velocity are normalised with respect to the stratification profile and the speed of sound, respectively. The ratio given by η_k is an important parameter for the observational studies listed above. The Fourier transform of the normalised X-ray SB fluctuations $\bar{\text{SB}}_k$ are used to calculate $\bar{\rho}_k$ and then $v_{1,k}$ is calculated using eq. (16).

All the observational studies we mentioned above assume $\eta_k^2 \approx 1$, independent of k , \mathcal{M} and Fr_\perp . A value of $\eta_k^2 \approx 1$ was calibrated

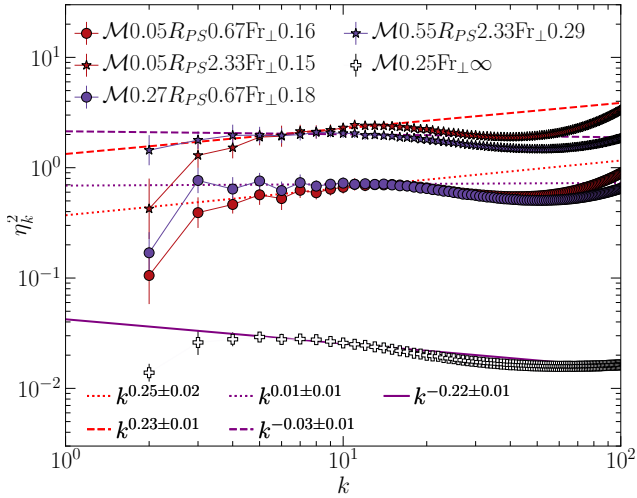


Figure 9. The ratio of density fluctuations to velocity power spectra, η_k^2 , defined in eq. (16), as a function of the wavenumber k , for our high-resolution, strongly stratified simulations. In this strongly stratified limit (which does not necessarily apply to the ICM in general; see Fig. 1 in MFS20), η_k^2 depends strongly on R_{PS} and weakly on k , \mathcal{M} and Fr_\perp .

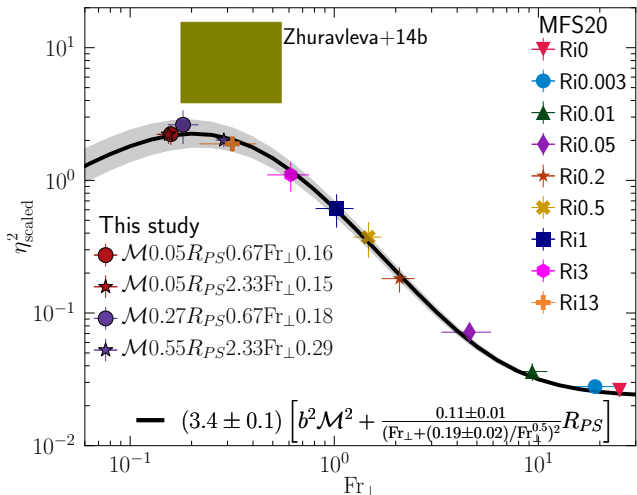


Figure 10. The scaled density to velocity fluctuation ratio (η_{scaled}^2) as a function of Fr_\perp for the high-resolution simulations from this study and from MFS20. The ratio (η_{scaled}^2) is averaged over the inertial range of turbulence ($6 \leq k \leq 15$). The fit (solid line) shown is plotted using $\mathcal{M} = 0.25$ and $R_{PS} = 2.33$, corresponding to the parameters used in MFS20. The ratio (η_{scaled}^2) roughly scales as $\sigma_{\rho}^2/\mathcal{M}^2$ and is independent of \mathcal{M} in the strongly stratified turbulence limit. We also show the values of η_{scaled}^2 and Fr_\perp clusters from Zhuravleva et al. (2014b) in the olive coloured shaded region. The values seem to be slightly larger than predicted by our scaling relation at low Fr_\perp . We discuss this discrepancy in the main text.

using cosmological simulations in Zhuravleva et al. (2014b) and large cluster scale (1000 kpc) simulations in Gaspari et al. (2014). In Mohapatra & Sharma (2019), we found $\eta_k^2 \propto \mathcal{M}^2$ through idealised box simulations of unstratified turbulence. We also noted that the amplitude of η_k^2 increases by two orders of magnitude on including cooling. In subsection 3.9.3 of MFS20, we studied the variation of η_k^2 for weakly and moderately stratified turbulence ($Fr_\perp \gtrsim 0.5$, $\mathcal{M} \approx 0.25$ and $R_{PS} = 2.33$). We showed that η_k^2 increases with

increasing stratification and reaches $\eta_k^2 \approx 1$ for $Fr_\perp \approx 0.7$. Here we have extended this study to the strongly stratified turbulence regime (up to $Fr_\perp \approx 0.1$).

In fig. 9, we show η_k^2 as a function of wavenumber k for our high-resolution, strongly stratified simulations. For reference, we show η_k^2 for the unstratified turbulence run ($Ri_0, Fr_\perp \rightarrow \infty$) from MFS20. The quantity η_k^2 is relatively flat with respect to k , for all of these simulations, which implies that $P(\delta\rho_k)$ and $P(\mathcal{M}_k)$ follow similar spectral scaling.

We also show η^2 , the amplitude of η_k^2 averaged over $6 \leq k \leq 15$ as a function of Fr_\perp in fig. 10 for the high-resolution simulations ($1024^2 \times 1536$) of this study and MFS20⁶. For the two simulations with $R_{PS} \neq 2.33$, we show $\eta_{\text{scaled}}^2 = \eta^2 \times (2.33/R_{PS})$. We fit the data using the expression for $\sigma_{\rho}^2/\mathcal{M}^2$ from eq. (13e) and $\mathcal{M} = 0.25$ and $R_{PS} = 2.33$, with ζ_1 and ζ_2 as fit parameters. The fitted factor of (3.4 ± 0.1) is close to the expected factor of 3 from the 3D to 1D conversion; see eq. (16). We have also plotted η_{scaled}^2 for cluster simulations from Zhuravleva et al. (2014b) in the olive coloured shaded region in fig. 10, which are slightly higher than our values and scaling relation. The differences in values of η_{scaled}^2 may arise from the choice of averaging regions, in this case 500 kpc regions in the clusters of Zhuravleva et al. 2014b. The density fluctuations in their study are also calculated as deviations from a beta-profile fit to these 500 kpc regions and thus are expected to be higher than our instantaneous z -slice averaging (described in section 2.3). In addition to this, since turbulence in these cosmological simulations is driven more naturally by galaxy mergers and in-falls, they may include compressive components (which are excluded in our simulations), increasing the value of the turbulence driving parameter b and generating larger density fluctuations. The cosmological simulations may also suffer from a lack of resolution on small scales and have a higher numerical viscosity compared to our idealised box simulations.

The amplitude of η_k^2 has the same dependence on \mathcal{M} , Fr_\perp , and R_{PS} , as the ratio of the rms fluctuations $\delta\rho^2/\mathcal{M}^2$. Since $\delta\rho_{\text{buoy}}^2$ is the main component of $\delta\rho^2$ for $Fr_\perp \approx 0.1$, η^2 scales similar to $\delta\rho_{\text{buoy}}^2/\mathcal{M}^2$. Hence η^2 is roughly independent of \mathcal{M} , weakly dependent on Fr_\perp (since σ_s versus Fr_\perp peaks at around $Fr_\perp \approx 0.1$), and linearly dependent on R_{PS} , in agreement with eq. (13d).

Combining the results of this work with those of Mohapatra & Sharma (2019) and MFS20, we have studied the variation of η_k^2 with \mathcal{M} , Fr_\perp , and R_{PS} , scanning the parameter space relevant for the ICM. We find that the ratio η_k^2 is almost invariant with the wavenumber k ⁷. The amplitude of η_k^2 varies as $\delta\rho^2/\mathcal{M}^2$. Based on eq. (13e) and the fit in fig. 10, we propose a new scaling relation for η^2 :

$$\eta^2 = (3.4 \pm 0.1) \left[b^2 \mathcal{M}^2 + \frac{(0.11 \pm 0.01) R_{PS}}{(Fr_\perp + (0.19 \pm 0.02) / \sqrt{Fr_\perp})^2} \right]. \quad (17)$$

For $Fr_\perp \lesssim 1$, η^2 approaches 1 and is independent of \mathcal{M} , which was the limit studied in Zhuravleva et al. (2014b) and Gaspari et al. (2014). However, as we showed in figure 1 of MFS20 (also in figure 2 of SZ19), the ICM can have Fr_\perp between 0.1–100. Thus, we suggest that observational studies use eq. (17) to obtain a more accurate estimate of turbulent velocities from density (surface

⁶ All simulations in MFS20 had $R_{PS} = 2.33$ and $\mathcal{M} \sim 0.25$.

⁷ Except for the heating and cooling simulations in Mohapatra & Sharma (2019), where switching on radiative cooling led to a steepening.

brightness) fluctuations. Since $\text{Fr}_\perp \lesssim 1$ also marks the onset of large-scale density anisotropy (see lower panels of fig. 1 and also fig. 10 in MFS20), one could use the peak value of η^2 , where it varies slowly with Fr_\perp for relating the ICM density and velocity fluctuations.

4 CAVEATS AND FUTURE WORK

In this section we discuss possible shortcomings of our work and possible methods to address some of them.

The buoyancy Reynolds number Re_{buoy} for stratified turbulence is given by $\text{Re}_\perp \text{Fr}_\perp^2$, where Re_\perp is the turbulent Reynolds number in the transverse direction. When $\text{Re}_{\text{buoy}} \gg 1$, viscous forces can be ignored on the integral scale ℓ_\perp (Davidson 2013). The ratio Re_\perp scales as $n^{4/3}$ in numerical simulations where n is the number of resolution elements (Frisch 1995; Haugen & Brandenburg 2004; Benzi et al. 2008; Federrath et al. 2011). Hence for low Fr_\perp simulations, $\text{Re}_{\text{buoy}} \approx 4096 \times \text{Fr}_\perp^2 \approx 10$ for $\text{Fr}_\perp 0.05$, using $n = 512$. Thus, we approach the limit $\text{Re}_{\text{buoy}} \approx 1$ for our strongly stratified simulations, implying that viscous forces are almost of the same order as the inertial forces on the integral scale for $\text{Fr}_\perp \approx 0.05$. Using higher grid resolution is one of the ways to avoid this issue.

In section 2.5.1, we mentioned that the positive z boundaries (at $z = 0.75$) are unstable for steep pressure profiles ($H_P < 0.25$). This happens because for the steepest pressure profiles with $H_P \approx 0.1$, the initial pressure varies by more than a factor of 10^6 across the entire domain. These steep gradients could possibly make the code numerically unstable near the low-pressure positive z boundary, especially when turbulent pressure becomes comparable to the thermal pressure. Using smaller box sizes (so that pressure values at the positive box boundary are higher) and/or higher resolution along the z direction is a possible solution to this problem. This method has been used by many fluid mechanics studies to study strongly stratified turbulence (Lindborg 2006; Brethouwer & Lindborg 2008).

In this paper, we have only studied solenoidally-driven stratified turbulence. The driving parameter b is also part of the scaling relation (Federrath et al. 2008, 2010). Compressively-driven turbulence is expected to generate larger density fluctuations and its effect is supposed to be captured by the driving parameter b , which we have not varied in any of our simulations. In nature, turbulence is supposed to be a mixture of compressive and solenoidal mode. Galaxy infall and mergers could possibly drive some compressive modes (Churazov et al. 2003; Federrath et al. 2017) in the ICM. Effects of different levels of compressively-driven turbulence would be an interesting follow-up study.

We have ignored the effects of radiative cooling, thermal conduction, and magnetic fields in this work. Radiative cooling (Mohapatra & Sharma 2019; Grete et al. 2020) and thermal conduction (Gaspari & Churazov 2013; Gaspari et al. 2014) have been shown to affect the $\delta\bar{\rho}-\mathcal{M}$ scaling relation. However, this additional physics is beyond the scope of the current paper and will be addressed in a follow-up study.

5 CONCLUSIONS

We have studied the parameter space relevant to subsonic, stratified turbulence in the ICM through idealised high-resolution hydrodynamic simulations. We have covered the parameter regime $0.05 < \text{Fr}_\perp < 12.0$, $0.05 \leq \mathcal{M} \leq 0.4$ and $0.33 \leq R_{PS} \leq 2.33$

through 96 simulations. The main results of this study are as follows:

(i) We have extended the scaling relation between the rms density fluctuations (denoted in log-scale by σ_s), the rms Mach number (\mathcal{M}), the perpendicular Froude number (Fr_\perp), and the ratio between pressure and entropy scale heights (R_{PS}) to the strong stratification limit ($\text{Fr}_\perp \ll 1$). The new scaling relation is $\sigma_s^2 = \ln \left[1 + b^2 \mathcal{M}^4 + \frac{0.10 \mathcal{M}^2 R_{PS}}{(\text{Fr}_\perp + 0.25/\sqrt{\text{Fr}_\perp})^2} \right]$. The density fluctuations increase with decreasing Fr_\perp for $\text{Fr}_\perp \gtrsim 0.2$, saturate and then decrease slowly for Fr_\perp . We have shown that the density fluctuations in all of our 100 simulations follow this scaling relation. Our results also qualitatively agree with the turbulence decay study in SZ19.

(ii) We have also extended the scaling of pressure fluctuations to the limit $\text{Fr}_\perp \ll 1$. We find that $\sigma_{\ln \bar{p}}$ is independent of the stratification parameters and depends only on \mathcal{M} . The scaling relation remains $\sigma_{\ln \bar{p}} = \ln \left[1 + b^2 \gamma^2 \mathcal{M}^4 \right]$. Since pressure fluctuations are unaffected by stratification, they can be used to obtain fairly accurate estimates of turbulent velocities through tSZ observations.

(iii) The ratio η_k between normalised one-dimensional Fourier density ($\bar{\rho}_k$) and velocity amplitudes ($v_{1,k}/c_s$) approximately scales as $\sigma_{\bar{\rho}}/\mathcal{M}$ and saturates to ≈ 1 at $\text{Fr}_\perp \approx 0.2$. The square of its amplitude is given by $\eta^2 = 3.4 \left[b^2 \mathcal{M}^2 + \frac{0.11 R_{PS}}{(\text{Fr}_\perp + 0.19/\sqrt{\text{Fr}_\perp})^2} \right]$.

(iv) The ratio between velocity components parallel and perpendicular to gravity (v_z/v_\perp) is roughly constant with respect to Fr_\perp for $\text{Fr}_\perp \gtrsim 1$, as expected for weak stratification. For $0.5 \lesssim \text{Fr}_\perp \lesssim 2$, the ratio weakly decreases with decreasing Fr_\perp , and for $\text{Fr}_\perp \lesssim 0.5$, it varies as $\text{Fr}_\perp^{0.7}$.

ACKNOWLEDGEMENTS

This work was carried out during the ongoing COVID-19 pandemic. The authors would like to acknowledge the health workers all over the world for their role in fighting in the frontline of this crisis. We thank the anonymous referee for their useful comments, which helped improve this work. RM acknowledges helpful discussions with Piyush Sharda. RM thanks Xun Shi and Irina Zhuravleva for providing data for subsection 3.3.6 and section 3.4, respectively and useful discussions. CF acknowledges funding provided by the Australian Research Council (Discovery Project DP170100603 and Future Fellowship FT180100495), and the Australia-Germany Joint Research Cooperation Scheme (UA-DAAD). PS acknowledges a Swarnajayanti Fellowship from the Department of Science and Technology, India (DST/SJF/PSA-03/2016-17). We further acknowledge high-performance computing resources provided by the Leibniz Rechenzentrum and the Gauss Centre for Supercomputing (grants pr32lo, pr48pi and GCS Large-scale project 10391), the Australian National Computational Infrastructure (grant ek9) in the framework of the National Computational Merit Allocation Scheme and the ANU Merit Allocation Scheme. The simulation software FLASH was in part developed by the DOE-supported Flash Center for Computational Science at the University of Chicago.

6 DATA AVAILABILITY

All the relevant data associated with this article is available upon request to the corresponding author.

7 ADDITIONAL LINKS

Movies of projected density and density fluctuations of different simulations are available at the following links on youtube:

- (i) [Movie](#) of the representative simulations used in fig. 1.
- (ii) [Movie](#) of low \mathcal{M} , low Fr_\perp simulations listed in table 2.
- (iii) [Movie](#) of two sample stratified turbulence decay simulations used in section 3.3.6.

REFERENCES

- Alam S., Guha A., Verma M. K., 2019, *Journal of Fluid Mechanics*, **875**, 961
- Angelinelli M., Vazza F., Giocoli C., Etori S., Jones T. W., Brunetti G., Brüggem M., Eckert D., 2020, *MNRAS*, **495**, 864
- Banerjee N., Sharma P., 2014, *MNRAS*, **443**, 687
- Bautz M. W., et al., 2009, *PASJ*, **61**, 1117
- Beattie J. R., Federrath C., Seta A., 2020, *MNRAS*,
- Benzi R., Biferale L., Fisher R. T., Kadanoff L. P., Lamb D. Q., Toschi F., 2008, *Phys. Rev. Lett.*, **100**, 234503
- Biffi V., et al., 2016, *ApJ*, **827**, 112
- Billant P., Chomaz J.-M., 2001, *Physics of Fluids*, **13**, 1645
- Bolgiano R. J., 1959, *Journal of Geophysical Research*, **64**, 2226
- Bolgiano R. J., 1962, *J. Geophys. Res.*, **67**, 3015
- Bouchut F., Klingenberg C., Waagan K., 2007, *Numerische Mathematik*, **108**, 7
- Bouchut F., Klingenberg C., Waagan K., 2010, *Numerische Mathematik*, **115**, 647
- Brethouwer G., Lindborg E., 2008, *Geophys. Res. Lett.*, **35**, L06809
- Carnevale G. F., Briscolini M., Orlandi P., 2001, *Journal of Fluid Mechanics*, **427**, 205
- Cavaliere A., Lapi A., Fusco-Femiano R., 2011, *A&A*, **525**, A110
- Churazov E., Sunyaev R., Forman W., Böhringer H., 2002, *MNRAS*, **332**, 729
- Churazov E., Forman W., Jones C., Böhringer H., 2003, *ApJ*, **590**, 225
- Cowley L. L., Hu E. M., Jenkins E. B., York D. G., 1983, *ApJ*, **272**, 29
- Davidson P. A., 2013, *Turbulence in Rotating, Stratified and Electrically Conducting Fluids*. Cambridge University Press, doi:10.1017/CBO9781139208673
- Dubey A., et al., 2008, in Pogorelov N. V., Audit E., Zank G. P., eds, *Astronomical Society of the Pacific Conference Series Vol. 385, Numerical Modeling of Space Plasma Flows*. p. 145
- Eswaran V., Pope S. B., 1988, *Computers and Fluids*, **16**, 257
- Federrath C., 2016, *Journal of Plasma Physics*, **82**, 535820601
- Federrath C., Banerjee S., 2015, *MNRAS*, **448**, 3297
- Federrath C., Klessen R. S., Schmidt W., 2008, *ApJ*, **688**, L79
- Federrath C., Roman-Duval J., Klessen R. S., Schmidt W., Mac Low M. M., 2010, *A&A*, **512**, A81
- Federrath C., Sur S., Schleicher D. R. G., Banerjee R., Klessen R. S., 2011, *ApJ*, **731**, 62
- Federrath C., et al., 2017, in Crocker R. M., Longmore S. N., Bicknell G. V., eds, *IAU Symposium Vol. 322, The Multi-Messenger Astrophysics of the Galactic Centre*. pp 123–128 (arXiv:1609.08726), doi:10.1017/S1743921316012357
- Feraco F., Marino R., Pumir A., Primavera L., Mininni P. D., Pouquet A., Rosenberg D., 2018, arXiv e-prints, p. arXiv:1806.00342
- Frisch U., 1995, *Turbulence*
- Fryxell B., et al., 2000, *The Astrophysical Journal Supplement Series*, **131**, 273
- Gaspari M., Churazov E., 2013, *A&A*, **559**, A78
- Gaspari M., Churazov E., Nagai D., Lau E. T., Zhuravleva I., 2014, *A&A*, **569**, A67
- George M. R., Fabian A. C., Sanders J. S., Young A. J., Russell H. R., 2009, *MNRAS*, **395**, 657
- Goldreich P., Keeley D. A., 1977, *ApJ*, **212**, 243
- Grete P., O’Shea B. W., Beckwith K., 2020, *ApJ*, **889**, 19
- Haugen N. E. L., Brandenburg A., 2004, *Phys. Rev. E*, **70**, 026405
- Herring J. R., Kimura Y., 2013, *Physica Scripta Volume T*, **155**, 014031
- Hillel S., Soker N., 2020, *ApJ*, **896**, 104
- Hitomi Collaboration 2016, *Nature*, **535**, 117
- Hu Y., Lazarian A., Li Y., Zhuravleva I., Gendron-Marsolais M.-L., 2020, *ApJ*, **901**, 162
- Khatri R., Gaspari M., 2016, *MNRAS*, **463**, 655
- Kim W.-T., Narayan R., 2003, *ApJ*, **596**, L139
- Kumar A., Chatterjee A. G., Verma M. K., 2014, *Phys. Rev. E*, **90**, 023016
- Li Y., et al., 2020, *ApJ*, **889**, L1
- Lindborg E., 2006, *Journal of Fluid Mechanics*, **550**, 207
- Loewenstein M., Fabian A. C., 1990, *MNRAS*, **242**, 120
- McDonald M., Veilleux S., Rupke D. S. N., Mushotzky R., 2010, *ApJ*, **721**, 1262
- Mohapatra R., Sharma P., 2019, *MNRAS*, **484**, 4881
- Mohapatra R., Federrath C., Sharma P., 2020, *MNRAS*, **493**, 5838
- Mroczkowski T., et al., 2019, *Space Sci. Rev.*, **215**, 17
- Nelson K., Lau E. T., Nagai D., 2014, *ApJ*, **792**, 25
- Newville M., Stensitzki T., Allen D. B., Rawlik M., Ingargiola A., Nelson A., 2016, Lmfit: Non-Linear Least-Square Minimization and Curve-Fitting for Python (ascl:1606.014)
- Nolan C. A., Federrath C., Sutherland R. S., 2015, *MNRAS*, **451**, 1380
- Olivares V., et al., 2019, *A&A*, **631**, A22
- Omma H., Binney J., Bryan G., Slyz A., 2004, *MNRAS*, **348**, 1105
- Parmentier V., Showman A. P., Lian Y., 2013, *A&A*, **558**, A91
- Price D. J., Federrath C., Brunt C. M., 2011, *ApJ*, **727**, L21
- Rorai C., Mininni P. D., Pouquet A., 2014, *Phys. Rev. E*, **89**, 043002
- Rudie G. C., et al., 2012, *ApJ*, **750**, 67
- Sarazin C. L., O’Connell R. W., McNamara B. R., 1992, *ApJ*, **397**, L31
- Schmidt W., Hillebrandt W., Niemeier J. C., 2006, *Computers & Fluids*, **35**, 353
- Schuecker P., Finoguenov A., Miniati F., Böhringer H., Briel U. G., 2004, *A&A*, **426**, 387
- Shi X., Zhang C., 2019, *MNRAS*, **487**, 1072
- Simionescu A., Tremblay G., Werner N., Canning R. E. A., Allen S. W., Oonk J. B. R., 2018, *MNRAS*, **475**, 3004
- Simionescu A., et al., 2019, *Space Sci. Rev.*, **215**, 24
- Skoutnev V., Squire J., Bhattacharjee A., 2020, arXiv e-prints, p. arXiv:2008.01025
- Stein R. F., 1967, *Sol. Phys.*, **2**, 385
- Vantyghem A. N., et al., 2019, *ApJ*, **870**, 57
- Waagan K., Federrath C., Klingenberg C., 2011, *Journal of Computational Physics*, **230**, 3331
- Zeldovich Y. B., Sunyaev R. A., 1969, *Ap&SS*, **4**, 301
- Zhuravleva I., Churazov E., Kravtsov A., Lau E. T., Nagai D., Sunyaev R., 2013, *MNRAS*, **428**, 3274
- Zhuravleva I., et al., 2014a, *Nature*, **515**, 85
- Zhuravleva I., et al., 2014b, *ApJ*, **788**, L13
- Zhuravleva I., et al., 2015, *MNRAS*, **450**, 4184
- Zhuravleva I., Allen S. W., Mantz A., Werner N., 2018, *ApJ*, **865**, 53
- Zhuravleva I., Churazov E., Schekochihin A. A., Allen S. W., Vikhlinin A., Werner N., 2019, *Nature Astronomy*, **3**, 832

APPENDIX A

Figure A1 shows the relation between σ_s^2 and σ_ρ^2 . The relation $\sigma_s^2 = \ln\left(1 + \sigma_\rho^2\right)$ holds for log-normal distributions of density and/or small density fluctuations ($\sigma_\rho \ll 1$) (Price et al. 2011). We use this relation to explain the scaling of σ_s^2 based on the turbulent and buoyant components of σ_ρ^2 in our study.

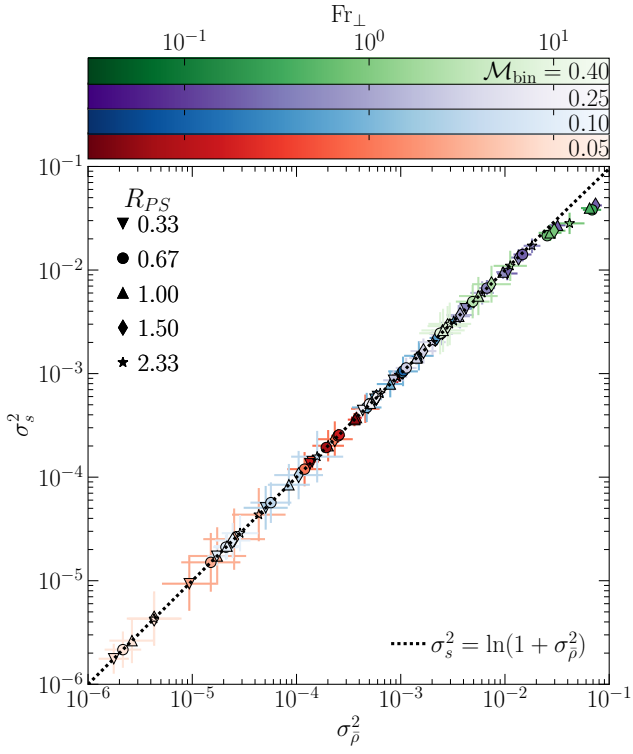


Figure A1. The spread in $\ln \rho$ (σ_s^2) as a function of the width in ρ (σ_ρ^2) for all our runs. The symbol shape corresponds to R_{PS} , the colour to the Mach number, and the shading to Fr_\perp . The data is fit well by $\sigma_s^2 = \ln(1 + \sigma_\rho^2)$, as discussed in the last paragraph of section 3.3.2.

APPENDIX B

Table B1 provides a long version of table 1, listing all the simulations, including all input parameters and relevant calculated/output variables.

Table B1: Full list of simulations

\mathcal{M}_{bin}	H_ρ	H_P	Resolution	Fr_\perp	\mathcal{M}	σ_s^2	$\sigma_{\ln \bar{P}}^2$
0.01	8.00	8.00	$512^2 \times 768$	$3.4^{+0.3}_{-0.3} \times 10^{-1}$	0.0087 ± 0.0003	$1.1^{+0.1}_{-0.2} \times 10^{-5}$	$1.4^{+0.3}_{-0.4} \times 10^{-9}$
0.01	4.00	4.00	$512^2 \times 768$	$1.8^{+0.2}_{-0.2} \times 10^{-1}$	0.0089 ± 0.0005	$1.1^{+0.1}_{-0.2} \times 10^{-5}$	$1.4^{+0.3}_{-0.3} \times 10^{-9}$
0.01	2.00	2.00	$512^2 \times 768$	$9.4^{+1.3}_{-1.5} \times 10^{-2}$	0.0098 ± 0.0008	$7.4^{+1.2}_{-1.5} \times 10^{-6}$	$1.6^{+0.6}_{-0.4} \times 10^{-9}$
0.01	1.00	1.00	$512^2 \times 768$	$4.4^{+0.6}_{-0.7} \times 10^{-2}$	0.010 ± 0.001	$6.4^{+1.1}_{-1.4} \times 10^{-6}$	$2.5^{+0.6}_{-0.8} \times 10^{-9}$
0.05	17.32	13.86	$256^2 \times 384$	$9.5^{+2.2}_{-2.9} \times 10^0$	0.053 ± 0.005	$1.7^{+0.5}_{-0.8} \times 10^{-6}$	$2.0^{+0.4}_{-0.5} \times 10^{-6}$
0.05	5.48	4.38	$256^2 \times 384$	$2.7^{+0.6}_{-0.9} \times 10^0$	0.053 ± 0.005	$9.1^{+4.3}_{-8.1} \times 10^{-6}$	$2.0^{+0.5}_{-0.5} \times 10^{-6}$
0.05	1.73	1.39	$256^2 \times 384$	$4.8^{+0.6}_{-0.7} \times 10^{-1}$	0.047 ± 0.005	$1.4^{+0.3}_{-0.3} \times 10^{-4}$	$1.3^{+0.3}_{-0.3} \times 10^{-6}$
0.05	0.55	0.44	$256^2 \times 384$	$1.6^{+0.4}_{-0.5} \times 10^{-1}$	0.050 ± 0.008	$1.3^{+0.2}_{-0.2} \times 10^{-4}$	$1.1^{+0.2}_{-0.3} \times 10^{-6}$
0.05	21.33	21.33	$256^2 \times 384$	$1.1^{+0.3}_{-0.4} \times 10^1$	0.053 ± 0.005	$2.1^{+0.7}_{-1.1} \times 10^{-6}$	$2.2^{+0.5}_{-0.6} \times 10^{-6}$
0.05	6.39	6.39	$256^2 \times 384$	$3.0^{+0.7}_{-0.8} \times 10^0$	0.053 ± 0.005	$1.5^{+0.7}_{-1.4} \times 10^{-5}$	$2.2^{+0.4}_{-0.5} \times 10^{-6}$
0.05	3.00	3.00	$256^2 \times 384$	$9.8^{+1.8}_{-2.2} \times 10^{-1}$	0.051 ± 0.005	$1.2^{+0.4}_{-0.6} \times 10^{-4}$	$1.8^{+0.4}_{-0.4} \times 10^{-6}$
0.05	1.96	1.96	$256^2 \times 384$	$4.9^{+0.7}_{-0.8} \times 10^{-1}$	0.048 ± 0.005	$2.5^{+0.5}_{-0.6} \times 10^{-4}$	$1.2^{+0.3}_{-0.5} \times 10^{-6}$
0.05	0.62	0.62	$512^2 \times 768$	$1.6^{+0.4}_{-0.5} \times 10^{-1}$	0.050 ± 0.008	$2.5^{+0.4}_{-0.4} \times 10^{-4}$	$1.0^{+0.3}_{-0.3} \times 10^{-6}$
0.05	0.62	0.62	$1024^2 \times 1536$	$1.6^{+0.2}_{-0.2} \times 10^{-1}$	0.050 ± 0.004	$2.4^{+0.4}_{-0.4} \times 10^{-4}$	$1.1^{+0.2}_{-0.3} \times 10^{-6}$
0.05	0.28	0.28	$512^2 \times 768$	$7.2^{+1.1}_{-1.3} \times 10^{-2}$	0.057 ± 0.010	$1.9^{+0.3}_{-0.3} \times 10^{-4}$	$2.0^{+0.5}_{-0.5} \times 10^{-6}$
0.05	21.87	26.25	$256^2 \times 384$	$1.1^{+0.2}_{-0.3} \times 10^1$	0.053 ± 0.005	$2.5^{+1.0}_{-1.8} \times 10^{-6}$	$2.1^{+0.5}_{-0.6} \times 10^{-6}$
0.05	7.14	8.57	$256^2 \times 384$	$3.1^{+0.7}_{-0.9} \times 10^0$	0.053 ± 0.005	$1.7^{+0.8}_{-1.6} \times 10^{-5}$	$2.1^{+0.4}_{-0.6} \times 10^{-6}$
0.05	3.00	3.60	$256^2 \times 384$	$9.5^{+1.7}_{-2.1} \times 10^{-1}$	0.051 ± 0.005	$2.0^{+0.6}_{-0.9} \times 10^{-4}$	$1.9^{+0.4}_{-0.4} \times 10^{-6}$
0.05	2.00	2.40	$256^2 \times 384$	$5.0^{+0.7}_{-0.8} \times 10^{-1}$	0.048 ± 0.005	$3.5^{+0.7}_{-0.9} \times 10^{-4}$	$1.3^{+0.3}_{-0.3} \times 10^{-6}$
0.05	0.60	0.72	$512^2 \times 768$	$1.5^{+0.4}_{-0.6} \times 10^{-1}$	0.051 ± 0.008	$3.7^{+0.6}_{-0.7} \times 10^{-4}$	$1.1^{+0.2}_{-0.3} \times 10^{-6}$
0.05	0.20	0.24	$512^2 \times 768$	$5.2^{+0.8}_{-0.9} \times 10^{-2}$	0.061 ± 0.011	$3.6^{+0.5}_{-0.6} \times 10^{-4}$	$4.4^{+1.1}_{-1.4} \times 10^{-6}$
0.05	17.78	26.67	$256^2 \times 384$	$8.8^{+2.2}_{-2.9} \times 10^0$	0.053 ± 0.005	$4.2^{+1.9}_{-3.7} \times 10^{-6}$	$2.1^{+0.5}_{-0.6} \times 10^{-6}$
0.05	7.14	10.71	$256^2 \times 384$	$3.2^{+0.7}_{-0.9} \times 10^0$	0.053 ± 0.005	$2.5^{+1.2}_{-2.5} \times 10^{-5}$	$2.1^{+0.4}_{-0.6} \times 10^{-6}$
0.05	3.20	4.80	$256^2 \times 384$	$1.1^{+0.2}_{-0.3} \times 10^0$	0.051 ± 0.005	$2.3^{+0.8}_{-1.2} \times 10^{-4}$	$1.9^{+0.4}_{-0.6} \times 10^{-6}$
0.05	2.00	3.00	$256^2 \times 384$	$5.0^{+0.6}_{-0.7} \times 10^{-1}$	0.047 ± 0.004	$4.8^{+1.0}_{-1.2} \times 10^{-4}$	$1.2^{+0.3}_{-0.4} \times 10^{-6}$
0.05	0.62	0.93	$512^2 \times 768$	$1.6^{+0.4}_{-0.6} \times 10^{-1}$	0.050 ± 0.008	$5.8^{+0.9}_{-1.1} \times 10^{-4}$	$1.1^{+0.3}_{-0.3} \times 10^{-6}$
0.05	0.20	0.30	$512^2 \times 768$	$5.5^{+0.8}_{-1.0} \times 10^{-2}$	0.063 ± 0.011	$5.8^{+0.9}_{-0.9} \times 10^{-4}$	$3.8^{+0.8}_{-1.0} \times 10^{-6}$
0.05	20.00	39.99	$256^2 \times 384$	$1.0^{+0.2}_{-0.3} \times 10^1$	0.053 ± 0.005	$4.1^{+1.8}_{-3.3} \times 10^{-6}$	$2.1^{+0.4}_{-0.5} \times 10^{-6}$
0.05	6.67	13.33	$256^2 \times 384$	$3.1^{+0.7}_{-0.9} \times 10^0$	0.052 ± 0.005	$4.3^{+2.0}_{-3.6} \times 10^{-5}$	$2.0^{+0.5}_{-0.6} \times 10^{-6}$
0.05	2.75	5.50	$256^2 \times 384$	$8.8^{+1.4}_{-1.7} \times 10^{-1}$	0.050 ± 0.005	$4.5^{+1.3}_{-1.8} \times 10^{-4}$	$1.8^{+0.4}_{-0.5} \times 10^{-6}$
0.05	1.25	2.50	$256^2 \times 384$	$3.1^{+0.3}_{-0.4} \times 10^{-1}$	0.046 ± 0.005	$9.6^{+1.6}_{-1.9} \times 10^{-4}$	$1.1^{+0.3}_{-0.4} \times 10^{-6}$
0.05	0.58	1.16	$512^2 \times 768$	$1.5^{+0.5}_{-0.7} \times 10^{-1}$	0.050 ± 0.008	$9.2^{+1.5}_{-1.8} \times 10^{-4}$	$1.2^{+0.3}_{-0.4} \times 10^{-6}$
0.05	0.58	1.16	$1024^2 \times 1536$	$1.5^{+0.2}_{-0.2} \times 10^{-1}$	0.051 ± 0.007	$9.2^{+1.3}_{-1.7} \times 10^{-4}$	$1.2^{+0.3}_{-0.4} \times 10^{-6}$
0.05	0.20	0.40	$512^2 \times 768$	$5.9^{+1.0}_{-1.3} \times 10^{-2}$	0.064 ± 0.011	$9.2^{+1.2}_{-1.4} \times 10^{-4}$	$4.3^{+0.9}_{-1.1} \times 10^{-6}$
0.10	8.66	6.93	$256^2 \times 384$	$9.5^{+2.3}_{-3.1} \times 10^0$	0.104 ± 0.012	$1.7^{+0.4}_{-0.5} \times 10^{-5}$	$3.0^{+0.7}_{-1.0} \times 10^{-5}$
0.10	2.74	2.19	$256^2 \times 384$	$2.6^{+0.6}_{-0.8} \times 10^0$	0.103 ± 0.011	$5.0^{+2.0}_{-3.3} \times 10^{-5}$	$2.8^{+0.7}_{-0.9} \times 10^{-5}$
0.10	0.87	0.69	$256^2 \times 384$	$4.9^{+0.7}_{-0.8} \times 10^{-1}$	0.096 ± 0.009	$5.6^{+1.0}_{-1.2} \times 10^{-4}$	$2.2^{+0.5}_{-0.5} \times 10^{-5}$
0.10	0.27	0.22	$512^2 \times 768$	$1.6^{+0.3}_{-0.3} \times 10^{-1}$	0.102 ± 0.017	$6.0^{+1.0}_{-1.2} \times 10^{-4}$	$2.6^{+0.6}_{-0.8} \times 10^{-5}$
0.10	9.59	9.59	$256^2 \times 384$	$9.8^{+2.3}_{-3.0} \times 10^0$	0.105 ± 0.010	$2.1^{+0.6}_{-0.8} \times 10^{-5}$	$3.2^{+0.7}_{-0.9} \times 10^{-5}$

continued . . .

... continued

\mathcal{M}_{bin}	H_ρ	H_P	Resolution	Fr_\perp	\mathcal{M}	σ_s^2	$\sigma_{\ln \bar{P}}^2$
0.10	3.75	3.75	$256^2 \times 384$	$3.4_{+1.0}^{-0.8} \times 10^0$	0.105 ± 0.008	$5.6_{+3.4}^{-2.1} \times 10^{-5}$	$3.1_{+0.7}^{-0.5} \times 10^{-5}$
0.10	1.56	1.56	$256^2 \times 384$	$1.0_{+0.2}^{-0.2} \times 10^0$	0.100 ± 0.010	$4.6_{+2.0}^{-1.4} \times 10^{-4}$	$2.7_{+0.8}^{-0.6} \times 10^{-5}$
0.10	0.98	0.98	$256^2 \times 384$	$5.0_{+0.8}^{-0.7} \times 10^{-1}$	0.094 ± 0.009	$1.0_{+0.3}^{-0.2} \times 10^{-3}$	$2.0_{+0.6}^{-0.5} \times 10^{-5}$
0.10	0.22	0.22	$512^2 \times 768$	$1.2_{+0.2}^{-0.2} \times 10^{-1}$	0.114 ± 0.021	$1.1_{+0.2}^{-0.2} \times 10^{-3}$	$3.6_{+1.4}^{-1.0} \times 10^{-5}$
0.10	11.18	13.41	$256^2 \times 384$	$1.1_{+0.4}^{-0.3} \times 10^1$	0.105 ± 0.011	$2.1_{+0.8}^{-0.6} \times 10^{-5}$	$3.2_{+1.0}^{-0.7} \times 10^{-5}$
0.10	3.76	4.51	$256^2 \times 384$	$3.2_{+0.9}^{-0.7} \times 10^0$	0.105 ± 0.011	$8.3_{+5.3}^{-3.2} \times 10^{-5}$	$3.3_{+1.0}^{-0.8} \times 10^{-5}$
0.10	1.50	1.80	$256^2 \times 384$	$9.0_{+1.8}^{-1.5} \times 10^{-1}$	0.100 ± 0.008	$7.8_{+3.0}^{-2.2} \times 10^{-4}$	$2.9_{+0.7}^{-0.6} \times 10^{-5}$
0.10	1.00	1.20	$256^2 \times 384$	$5.0_{+0.8}^{-0.7} \times 10^{-1}$	0.094 ± 0.008	$1.4_{+0.3}^{-0.3} \times 10^{-3}$	$1.9_{+0.6}^{-0.4} \times 10^{-5}$
0.10	0.22	0.26	$512^2 \times 768$	$1.2_{+0.2}^{-0.2} \times 10^{-1}$	0.114 ± 0.020	$1.4_{+0.3}^{-0.2} \times 10^{-3}$	$2.8_{+0.9}^{-0.7} \times 10^{-5}$
0.10	10.61	15.92	$256^2 \times 384$	$1.1_{+0.4}^{-0.3} \times 10^1$	0.105 ± 0.010	$2.4_{+1.2}^{-0.8} \times 10^{-5}$	$3.1_{+0.8}^{-0.7} \times 10^{-5}$
0.10	3.75	5.62	$256^2 \times 384$	$3.3_{+0.8}^{-0.7} \times 10^0$	0.104 ± 0.009	$1.0_{+0.8}^{-0.4} \times 10^{-4}$	$3.0_{+0.7}^{-0.6} \times 10^{-5}$
0.10	1.50	2.25	$256^2 \times 384$	$9.1_{+1.6}^{-1.4} \times 10^{-1}$	0.100 ± 0.007	$1.0_{+0.4}^{-0.3} \times 10^{-3}$	$3.0_{+0.7}^{-0.5} \times 10^{-5}$
0.10	0.98	1.47	$256^2 \times 384$	$4.8_{+0.6}^{-0.5} \times 10^{-1}$	0.096 ± 0.008	$2.2_{+0.5}^{-0.4} \times 10^{-3}$	$2.0_{+0.7}^{-0.5} \times 10^{-5}$
0.10	0.22	0.33	$512^2 \times 768$	$1.2_{+0.3}^{-0.2} \times 10^{-1}$	0.114 ± 0.021	$2.5_{+0.4}^{-0.4} \times 10^{-3}$	$3.2_{+1.1}^{-0.8} \times 10^{-5}$
0.10	10.00	20.00	$256^2 \times 384$	$1.1_{+0.4}^{-0.3} \times 10^1$	0.105 ± 0.010	$2.8_{+1.5}^{-1.0} \times 10^{-5}$	$3.2_{+0.9}^{-0.7} \times 10^{-5}$
0.10	3.50	7.00	$256^2 \times 384$	$3.3_{+0.9}^{-0.7} \times 10^0$	0.104 ± 0.009	$1.6_{+1.3}^{-0.7} \times 10^{-4}$	$3.1_{+0.9}^{-0.7} \times 10^{-5}$
0.10	1.50	3.00	$256^2 \times 384$	$9.7_{+1.9}^{-1.6} \times 10^{-1}$	0.099 ± 0.009	$1.5_{+0.6}^{-0.4} \times 10^{-3}$	$3.1_{+0.9}^{-0.7} \times 10^{-5}$
0.10	0.92	1.83	$256^2 \times 384$	$4.7_{+0.5}^{-0.5} \times 10^{-1}$	0.097 ± 0.008	$3.2_{+0.6}^{-0.5} \times 10^{-3}$	$2.2_{+0.7}^{-0.5} \times 10^{-5}$
0.10	0.20	0.40	$512^2 \times 768$	$1.1_{+0.3}^{-0.2} \times 10^{-1}$	0.114 ± 0.019	$4.7_{+0.8}^{-0.7} \times 10^{-3}$	$5.1_{+1.7}^{-1.3} \times 10^{-5}$
0.25	3.46	2.77	$256^2 \times 384$	$8.9_{+2.5}^{-1.9} \times 10^0$	0.244 ± 0.025	$4.3_{+1.2}^{-0.9} \times 10^{-4}$	$8.8_{+2.6}^{-2.0} \times 10^{-4}$
0.25	1.10	0.88	$256^2 \times 384$	$2.4_{+0.7}^{-0.6} \times 10^0$	0.244 ± 0.024	$8.5_{+2.6}^{-2.0} \times 10^{-4}$	$8.9_{+2.1}^{-1.7} \times 10^{-4}$
0.25	0.35	0.28	$256^2 \times 384$	$5.1_{+2.4}^{-1.6} \times 10^{-1}$	0.238 ± 0.024	$4.2_{+0.9}^{-0.7} \times 10^{-3}$	$1.1_{+0.4}^{-0.3} \times 10^{-3}$
0.25	0.12	0.10	$512^2 \times 768$	$1.6_{+0.2}^{-0.2} \times 10^{-1}$	0.206 ± 0.034	$2.5_{+0.5}^{-0.4} \times 10^{-3}$	$5.3_{+2.0}^{-1.5} \times 10^{-4}$
0.25	6.40	6.40	$256^2 \times 384$	$1.1_{+0.3}^{-0.2} \times 10^1$	0.248 ± 0.023	$5.0_{+0.9}^{-0.8} \times 10^{-4}$	$9.8_{+2.3}^{-1.8} \times 10^{-4}$
0.25	2.00	2.00	$256^2 \times 384$	$3.2_{+0.7}^{-0.6} \times 10^0$	0.250 ± 0.028	$1.1_{+0.3}^{-0.2} \times 10^{-3}$	$1.1_{+0.3}^{-0.2} \times 10^{-3}$
0.25	0.75	0.75	$256^2 \times 384$	$1.2_{+0.3}^{-0.2} \times 10^0$	0.236 ± 0.023	$2.4_{+0.9}^{-0.6} \times 10^{-3}$	$8.0_{+2.4}^{-1.8} \times 10^{-4}$
0.25	0.39	0.39	$256^2 \times 384$	$5.1_{+4.5}^{-2.1} \times 10^{-1}$	0.233 ± 0.021	$6.6_{+1.8}^{-1.4} \times 10^{-3}$	$8.1_{+2.3}^{-1.8} \times 10^{-4}$
0.25	0.12	0.12	$512^2 \times 768$	$1.8_{+0.2}^{-0.2} \times 10^{-1}$	0.266 ± 0.043	$8.5_{+1.9}^{-1.5} \times 10^{-3}$	$1.2_{+0.3}^{-0.3} \times 10^{-3}$
0.25	0.12	0.12	$1024^2 \times 1536$	$1.8_{+0.2}^{-0.2} \times 10^{-1}$	0.267 ± 0.009	$8.5_{+1.6}^{-1.4} \times 10^{-3}$	$1.2_{+0.3}^{-0.2} \times 10^{-3}$
0.25	7.00	8.40	$256^2 \times 384$	$1.2_{+0.2}^{-0.2} \times 10^1$	0.248 ± 0.020	$5.1_{+0.9}^{-0.8} \times 10^{-4}$	$9.7_{+2.1}^{-1.7} \times 10^{-4}$
0.25	2.00	2.40	$256^2 \times 384$	$3.1_{+0.7}^{-0.5} \times 10^0$	0.248 ± 0.023	$1.4_{+0.3}^{-0.3} \times 10^{-3}$	$1.0_{+0.2}^{-0.2} \times 10^{-3}$
0.25	0.75	0.90	$256^2 \times 384$	$1.1_{+0.3}^{-0.2} \times 10^0$	0.237 ± 0.024	$3.5_{+1.3}^{-0.9} \times 10^{-3}$	$8.4_{+2.7}^{-2.0} \times 10^{-4}$
0.25	0.40	0.48	$256^2 \times 384$	$5.1_{+4.1}^{-2.1} \times 10^{-1}$	0.232 ± 0.021	$9.3_{+2.5}^{-1.8} \times 10^{-3}$	$7.7_{+2.6}^{-1.9} \times 10^{-4}$
0.25	0.10	0.12	$512^2 \times 768$	$1.9_{+0.2}^{-0.2} \times 10^{-1}$	0.362 ± 0.043	$2.3_{+0.5}^{-0.4} \times 10^{-2}$	$4.4_{+1.4}^{-1.0} \times 10^{-3}$
0.25	6.40	9.60	$256^2 \times 384$	$1.1_{+0.3}^{-0.2} \times 10^1$	0.252 ± 0.022	$5.9_{+1.2}^{-1.0} \times 10^{-4}$	$1.0_{+0.2}^{-0.2} \times 10^{-3}$
0.25	2.00	3.00	$256^2 \times 384$	$3.2_{+0.7}^{-0.5} \times 10^0$	0.249 ± 0.024	$1.6_{+0.6}^{-0.4} \times 10^{-3}$	$9.9_{+2.2}^{-1.8} \times 10^{-4}$
0.25	0.82	1.24	$256^2 \times 384$	$1.4_{+0.3}^{-0.3} \times 10^0$	0.236 ± 0.025	$3.6_{+1.4}^{-1.0} \times 10^{-3}$	$8.4_{+3.0}^{-2.2} \times 10^{-4}$
0.25	0.39	0.59	$256^2 \times 384$	$4.9_{+3.2}^{-1.8} \times 10^{-1}$	0.231 ± 0.023	$1.3_{+0.4}^{-0.3} \times 10^{-2}$	$7.6_{+2.2}^{-1.7} \times 10^{-4}$
0.25	0.10	0.15	$512^2 \times 768$	$2.2_{+0.3}^{-0.2} \times 10^{-1}$	0.449 ± 0.053	$6.7_{+1.4}^{-1.1} \times 10^{-2}$	$1.2_{+0.3}^{-0.3} \times 10^{-2}$
0.25	6.00	12.00	$256^2 \times 384$	$1.1_{+0.2}^{-0.2} \times 10^1$	0.251 ± 0.023	$6.4_{+1.3}^{-1.1} \times 10^{-4}$	$1.0_{+0.2}^{-0.2} \times 10^{-3}$
0.25	2.00	4.00	$256^2 \times 384$	$3.3_{+0.6}^{-0.5} \times 10^0$	0.247 ± 0.021	$2.0_{+0.7}^{-0.5} \times 10^{-3}$	$9.7_{+2.0}^{-1.6} \times 10^{-4}$
0.25	0.75	1.50	$256^2 \times 384$	$1.3_{+0.3}^{-0.2} \times 10^0$	0.235 ± 0.024	$5.9_{+2.3}^{-1.6} \times 10^{-3}$	$7.8_{+2.8}^{-2.1} \times 10^{-4}$

continued ...

... continued

\mathcal{M}_{bin}	H_ρ	H_P	Resolution	Fr_\perp	\mathcal{M}	σ_s^2	$\sigma_{\ln \bar{P}}^2$
0.25	0.37	0.73	$256^2 \times 384$	$5.2_{-2.0}^{+1.4} \times 10^{-1}$	0.232 ± 0.022	$1.7_{-0.5}^{+0.4} \times 10^{-2}$	$8.0_{-2.2}^{+1.7} \times 10^{-4}$
0.25	0.10	0.20	$512^2 \times 768$	$2.9_{-0.7}^{+0.5} \times 10^{-1}$	0.536 ± 0.070	$1.4_{-0.3}^{+0.3} \times 10^{-1}$	$3.0_{-0.9}^{+0.7} \times 10^{-2}$
0.25	0.10	0.20	$1024^2 \times 1536$	$2.9_{-0.3}^{+0.3} \times 10^{-1}$	0.550 ± 0.083	$1.4_{-0.4}^{+0.3} \times 10^{-1}$	$3.2_{-0.9}^{+0.7} \times 10^{-2}$
0.40	1.75	1.75	$512^2 \times 768$	$7.4_{-1.7}^{+1.4} \times 10^0$	0.365 ± 0.069	$2.4_{-1.5}^{+0.9} \times 10^{-3}$	$4.3_{-3.2}^{+1.8} \times 10^{-3}$
0.40	0.70	0.70	$512^2 \times 768$	$2.7_{-0.8}^{+0.6} \times 10^0$	0.371 ± 0.065	$4.9_{-2.5}^{+1.6} \times 10^{-3}$	$5.4_{-3.2}^{+2.0} \times 10^{-3}$
0.40	0.30	0.30	$512^2 \times 768$	$7.3_{-4.7}^{+2.5} \times 10^{-1}$	0.400 ± 0.067	$2.2_{-0.6}^{+0.4} \times 10^{-2}$	$1.3_{-0.5}^{+0.3} \times 10^{-2}$
0.40	0.15	0.15	$512^2 \times 768$	$3.3_{-0.5}^{+0.4} \times 10^{-1}$	0.402 ± 0.079	$3.2_{-1.0}^{+0.8} \times 10^{-2}$	$1.1_{-0.4}^{+0.3} \times 10^{-2}$
0.40	1.75	2.10	$512^2 \times 768$	$7.8_{-1.7}^{+1.4} \times 10^0$	0.367 ± 0.071	$2.6_{-1.8}^{+1.0} \times 10^{-3}$	$4.4_{-3.2}^{+1.8} \times 10^{-3}$
0.40	0.70	0.84	$512^2 \times 768$	$2.8_{-0.8}^{+0.6} \times 10^0$	0.378 ± 0.065	$5.5_{-3.3}^{+2.0} \times 10^{-3}$	$5.9_{-3.4}^{+2.1} \times 10^{-3}$
0.40	0.30	0.36	$512^2 \times 768$	$7.7_{-4.0}^{+2.3} \times 10^{-1}$	0.402 ± 0.068	$2.3_{-0.7}^{+0.5} \times 10^{-2}$	$1.2_{-0.5}^{+0.3} \times 10^{-2}$
0.40	0.17	0.20	$512^2 \times 768$	$4.2_{-0.9}^{+0.7} \times 10^{-1}$	0.436 ± 0.090	$4.5_{-1.3}^{+1.0} \times 10^{-2}$	$1.7_{-0.7}^{+0.5} \times 10^{-2}$
0.40	1.37	2.06	$512^2 \times 768$	$6.8_{-1.7}^{+1.3} \times 10^0$	0.365 ± 0.075	$2.9_{-1.7}^{+1.1} \times 10^{-3}$	$4.3_{-3.3}^{+1.9} \times 10^{-3}$
0.40	0.60	0.90	$512^2 \times 768$	$2.6_{-0.7}^{+0.6} \times 10^0$	0.383 ± 0.069	$7.1_{-4.2}^{+2.6} \times 10^{-3}$	$6.6_{-3.7}^{+2.3} \times 10^{-3}$
0.40	0.30	0.45	$512^2 \times 768$	$9.0_{-3.0}^{+2.2} \times 10^{-1}$	0.400 ± 0.070	$2.5_{-0.8}^{+0.6} \times 10^{-2}$	$1.2_{-0.6}^{+0.4} \times 10^{-2}$
0.40	0.14	0.21	$512^2 \times 768$	$4.7_{-1.1}^{+0.8} \times 10^{-1}$	0.543 ± 0.080	$9.0_{-1.8}^{+1.5} \times 10^{-2}$	$4.1_{-1.1}^{+0.8} \times 10^{-2}$
0.40	1.33	2.67	$512^2 \times 768$	$7.3_{-1.7}^{+1.4} \times 10^0$	0.367 ± 0.070	$3.0_{-2.0}^{+1.2} \times 10^{-3}$	$4.7_{-3.5}^{+2.0} \times 10^{-3}$
0.40	0.50	1.00	$512^2 \times 768$	$2.2_{-0.6}^{+0.5} \times 10^0$	0.390 ± 0.067	$1.1_{-0.5}^{+0.3} \times 10^{-2}$	$7.4_{-4.0}^{+2.5} \times 10^{-3}$
0.40	0.27	0.54	$512^2 \times 768$	$9.5_{-3.1}^{+2.3} \times 10^{-1}$	0.397 ± 0.077	$3.3_{-1.3}^{+0.9} \times 10^{-2}$	$1.5_{-0.8}^{+0.5} \times 10^{-2}$
0.40	0.12	0.25	$512^2 \times 768$	$7.1_{-9.1}^{+3.5} \times 10^{-1}$	0.585 ± 0.153	$1.0_{-0.4}^{+0.3} \times 10^{-1}$	$4.9_{-2.9}^{+1.8} \times 10^{-2}$

This paper has been typeset from a $\text{\TeX}/\text{\LaTeX}$ file prepared by the author.